Monitoring and Modeling Drainage Network Contraction and Dry Down in Mediterranean Headwater Catchments

Alfonso Senatore[1] , **Massimo Micieli[1,2], Alessio Liotti[1], Nicola Durighetto[2]** , **Giuseppe Mendicino[1]** , **and Gianluca Botter[2]**

[1]Department of Environmental Engineering, University of Calabria, Rende, Italy, [2]Department of Civil, Environmental and Architectural Engineering, University of Padua, Padua, Italy

Abstract Understanding the expansion and contraction dynamics of flowing drainage networks is important for many research fields like ecology, hydrology, and biogeochemistry. This study analyzes for the first time the network shrinking and dry down in two seasonally dry hot-summer Mediterranean catchments (overall area 1.15 km^2) using a comprehensive approach based on monitoring and modeling of the flowing network. A field campaign consisting of 19 subweekly visual surveys was carried out in the early summer of 2019. These observations were used to calibrate and validate an integrated model aimed to estimate the time evolution of the total flowing drainage network length based on meteorological drivers and define the position of the stretches with flowing water based on topographic and geological information. We used a statistical model to describe the observed variations in the total flowing length based on the accumulated difference between antecedent precipitation and evapotranspiration. The study emphasizes the relevant role of evapotranspiration in the seasonal network contraction. Then, we modeled spatial patterns of the flowing channels using an empirical approach based on topographic data, achieving satisfactory performances. Nevertheless, the performance further increased when site-specific geological information was integrated into the model, leading to accuracies up to 92% for cell-by-cell comparisons. The proposed methodology, which combines meteorological, topographic, and geological information in a sequential manner, was able to accurately represent the space-time dynamics of the flowing drainage network in the study area, proving to be an effective and flexible tool for investigating network dynamics in temporary streams.

1. Introduction

Virtually all watercourses experience discontinuous flows along their drainage network. Nonpermanent streams can be observed not only in dry regions but also in most low-order channels of the network, representing more than 89% of the global river network (G. H. Allen et al., 2018; Downing et al., 2012), even in wet climates (Datry et al., 2014; Durighetto et al., 2020; Fritz et al., 2013; Larned et al., 2010; Tooth, 2000). While the potential or geomorphic river network, here defined as the set of incised channels with banks and a definable channel head (Zimmer & McGlynn, 2017), can be considered as static, its temporary flowing portion is highly unsteady. It responds to weather and climate changes at different time scales, from single events to multiyear scales (Costigan et al., 2016), causing spatial and temporal variability of local hydraulic conditions. The temporary portions of rivers entail stream network expansion, contraction, and fragmentation with important implications across many research fields. In particular, stream intermittency is important for freshwater ecology (Datry et al., 2014; Vander Vorste et al., 2019), biogeochemical cycles (Abbott et al., 2016; Berger et al., 2017; Dupas et al., 2019), carbon dioxide emissions (Boodoo et al., 2017; Datry et al., 2018; Schiller et al., 2014), hydrology (e.g., Godsey & Kirchner, 2014; C. Jensen et al., 2017; Mendicino & Colosimo, 2019), and watershed management and policy (Acuña et al., 2014; Nikolaidis et al., 2013).

Studying temporary rivers is particularly challenging for ecologists, who need to characterize "shifting mosaics" of lotic, lentic, and terrestrial habitats (Datry et al., 2016), and for hydrologists, who address the topic of "zero flow" in developing nonlinear and threshold-based approaches (e.g., Botter et al., 2009; McInerney et al., 2019; Mendicino & Senatore, 2013a; Zehe & Sivapalan, 2009). Temporary rivers are also an open issue for water policy. For example, dynamic streams are sought to be better integrated into the European Union Water Framework Directive 2000/60/EC (WFD; European Commission, 2000; Nikolaidis et al., 2013; Reyjol et al., 2014), especially in view of the increasing impact of climate change and land use development in

Mediterranean Europe (Skoulikidis et al., 2017), which are expected to shift permanent streams to temporary. In the Mediterranean region, stream types with extremely erratic flow regimes exist, often identified with specific names ("fiumara" in southern Italy; "wadi" in the Middle East and northern Africa) and characterized by specific geological, hydrological, and ecological traits.

Several pioneering studies of rivers with discontinuous flow were carried out in the 1960s and 1970s (Anderson & Burt, 1978; Blyth & Rodda, 1973; Day, 1978, 1980; Gregory & Gardiner, 1979; Gregory & Walling, 1968; Morgan, 1972; Roberts & Archibold, 1978), mainly for specific hydrological purposes (i.e., assessing the link between drainage density and the hydrological response to precipitation). Nevertheless, as soon as the hypothesis of a strong correlation between drainage density and streamflow dynamics was rejected, these early studies were largely abandoned (Godsey & Kirchner, 2014). Recently, the multifaceted implications of river network dynamics have contributed to a renewed interest in the scientific community for temporary streams. Table 1 shows a representative, although not exhaustive, selection of hydrological studies concerning river network dynamics monitoring (and modeling, in several cases) carried out in the last 20 years. Different monitoring approaches were adopted, including those that rely on stream gauges for long-term analyses (e.g., Costigan et al., 2015; Yu et al., 2018) to aerial or satellite images (e.g., Phillips et al., 2011; Wigington et al., 2005). However, given several technical issues (e.g., problems related to zero-flow stream gauge readings, Zimmer et al., 2020; or limits of aerial surveys, Spence & Mengistu, 2016; Tomaštík et al., 2019), the prevailing observation method is represented by visual surveys, sometimes aided by water presence sensors (Assendelft & van Meerveld, 2019; Goulsbra et al., 2014; C. K. Jensen et al., 2019; Kaplan et al., 2019; Paillex et al., 2020; Peirce & Lindsay, 2015) that can significantly increase the temporal resolution of the data sets.

Table 1 indicates that some studies have been carried out in temperate Mediterranean climates with cool wet winters and cold to warm dry summers. Among them, Godsey and Kirchner (2014) mapped active stream dynamics in four mainly snow-dominated Californian headwater catchments, focusing on the correlation between the active drainage network length (ADNL) and the specific discharge. In the same region (northern California), Lovill et al. (2018) monitored four headwater drainage networks in the early and late summer of different years, highlighting the importance of lithological characteristics for understanding drainage network persistency. However, intraseasonal changes in the active network within hot-summer Mediterranean climates, characterized by higher summer temperatures and an extensive seasonal imbalance between precipitation and evapotranspiration (ET), have not been monitored or modeled yet. In these conditions, the climate is expected to exert a primary control on flow intermittency and seasonal discharge dynamics (e.g., Garcia et al., 2017; Medici et al., 2008; Senatore et al., 2011). Zimmer and McGlynn (2017) also highlighted that in subtropical climates ET has a direct influence on the seasonality of runoff and its persistence. Likewise, the mean potential ET was one of the explanatory variables used by González-Ferreras and Barquín (2017) in their random forest-based classification model for identifying temporal or perennial river segments.

Linking the active river network length to weather variables is a straightforward and effective way to model its expansion and contraction dynamics. Many recent studies related the observed flowing network length directly to river discharge or water level (e.g., Doering et al., 2007; Prancevic & Kirchner, 2019; Shaw et al., 2017; Ward et al., 2018; Whiting & Godsey, 2016; Zimmer & McGlynn, 2017). However, streamflow itself is a dependent variable controlled by the meteorological input, and it is often controlled by precipitation patterns at time scales that differ from those relevant for active channel network dynamics (Durighetto et al., 2020; Shaw, 2016). Furthermore, hydrometric stations (with related reliable rating curves) are much less common than precipitation stations (Fekete & Vörösmarty, 2007; Kim & Sharma, 2019). Among the relatively few studies relating the active drainage network to weather and climatic drivers (Goulsbra et al., 2014; Jaeger et al., 2019; C. K. Jensen et al., 2018, 2019; Ward et al., 2018), Durighetto et al. (2020) were the first to explore the dependence of the active stream length on meteorological drivers aggregated at different time scales. In the study of Durighetto et al. (2020), the impact of ET on network dynamics was determined to be negligible because of the wet climate of their study area (annual rainfall >1,500 mm). To date, the extent to which this site-specific result can be extended to drier climate settings remains unknown.

A comprehensive modeling framework should be developed to estimate not only the total ADNL but also the corresponding spatial patterns of flowing river reaches. This goal is not trivial because the spatial

Table 1
Intercomparison of Recent Studies Addressing River Networks Dynamics Monitoring

Reference	Location	Climate	Observations	Areal extent	Temporal extent
Wigington et al. (2005)	Agricultural catchments in western Oregon, USA	Cool, wet winters and warm, dry summers, little snowfall	Aerial photographs	5 catchments from 21.6 to 47.8 km^2	Summer 1997, winter of 1998–1999
Malard et al. (2006)*	Braided glacial river in Switzerland	Alpine	24 field surveys; turbidity measurements	0.67 km^2	Monthly interval, from 1997 to 1999
Doering et al. (2007)*	River stretch of a river in north-eastern Italy	Mixed Alpine and Mediterranean Mean precipitation 2,150 mm year^{-1} Local climate is influenced by both snowmelt and precipitation regimes	Tens of field surveys	Unconstrained 41.5 km river segment	April 2003 to October 2004
Jaeger et al. (2007)	Forested landscapes in Washington State	Mean precipitation from 2,260 to 2,800 mm year^{-1}	Field mapping of contributing source areas (channel heads)	7 first-order streams with areas from 0.1 to 0.6 km^2	Nine months from February to September
Phillips et al. (2011)	Subarctic precambrian shield catchment (Canada) Mean precipitation about 300 mm year^{-1} Mean January temperature −26.8°C Mean July temperature 16.8°C		Multispectral satellite imagery and on-site measurements of storage according to land cover (four surveys)	Three subcatchments from 8 to 25 km^2	From May to August 2009
Godsey and Kirchner (2014)*	Four sites in Sierra Nevada and California Coast Range	Mediterranean, with three out of four sites snow dominated, mean precipitation from 1,000 to 1,200 mm year^{-1}	Field mapping of the stream networks (four surveys); discharge data available	From 3.6 to 27.2 km^2	Fall 2006, spring and fall 2007, and spring 2008
Goulsbra et al. (2014)*	Peatland headwater in UK Mean precipitation 1,513 mm year^{-1} Mean monthly temperature 7.0°C		Network of 40 sensors based on electrical resistance and discharge measures at the outlet	0.43 km^2	Two periods (autumn 2007 and summer 2008), overall almost 4 months
Ågren et al. (2015)	Boreal forest catchment in northern Sweden		9 surveys of stream heads of the catchment	121 stream heads	2013–2014
Costigan et al. (2015)*	Tallgrass prairie, Kansas Mean precipitation 780 mm year^{-1}	Temperate	Three headwater stream gages and a downstream gage	Headwater gages: about 1.2 km^2 Downstream gage: 10.6 km^2	25 years
Peirce and Lindsay (2015)	Ephemeral streams in southern Ontario Mean precipitation 771.4 mm year^{-1} Mean temperature 6.5°C		56 electrical resistance sensors	Three ephemeral subcatchments from 0.034 to 0.045 km^2	About 4 months during summer 2011

Table 1
Continued

Reference	Location	Climate	Observations	Areal extent	Temporal extent
Shaw (2016)*	Forested catchment in central New York State Mean precipitation presumably from 1,100 to 1,600 mm year^{-1}	Field mapping of flow length (12 surveys); discharge data	1.5 km^2	April–November 2013	
Whiting and Godsey (2016)*	Headwater streams in central Idaho Mean precipitation 700 mm year^{-1}, which primarily falls as snow in wet winter months	Three field surveys per catchment; discharge measurements	Four headwater catchments from 6.5 to 21.4 km^2	Spring and summer 2014	
González-Ferreras and Barquín (2017)*	Catchment in northern Spain draining into the Cantabric Sea Influence of both temperate oceanic and Mediterranean climate, precipitation over 2,000 mm year^{-1} above 1,000 m a.s.l.	149 surveys of different river segments over two seasons; aerial images from 2011 to 2014	1,200 km^2	Summer 2011 (normal year) and summer 2014 (wet year)	
C. Jensen et al. (2017)*	Forested headwater catchments in four physiographic provinces of the Appalachian Highlands, USA Mean precipitation from 1,000 to 1,460 mm year^{-1} Mean January temperature from −9°C to 3°C Mean July temperature from 18°C to 22°C	Field mapping of the stream networks (7 surveys); for 8 of the 12 study sites stream flow measurements available	12 headwater catchments with areas from 0.1 to 0.45 km^2 (except one catchment of 0.7 km^2)	Three surveys on June–July, August, September, October 2014, and November 2015	
Shaw et al. (2017)	Birch Creek watershed in the Catskill Mountains of New York State Humid continental Mean precipitation presumably from 1,100 to 1,600 mm year^{-1}	Field mapping of flow length; stream gaging	Three catchments from 4.62 to 11.53 km^2		
Zimmer and McGlynn (2017)*	Ephemeral-to-intermittent drainage network in the Piedmont region of North Carolina, USA Subtropical, humid climate Mean precipitation 1,136 mm year^{-1} Mean temperature 15.5°C	77 surface drainage network mapping campaigns over a wide range of runoff magnitudes; runoff and groundwater measurements	0.033 km^2	October 2014 to June 2016	
Floriancic et al. (2018)*	Alpine catchment, Switzerland Alpine Mean precipitation 1,738 mm year^{-1} Mean temperature 0.2°C	Seven discharge measures in four nested subcatchments; stream water electrical conductivity and water chemistry	4 subcatchments areas varying from 1.4 to 5.1 km^2; total area 14.4 km^2	One winter recession period (4 months)	
Lovill et al. (2018)*	Northern California Coast Range Mediterranean, with mean precipitation 2,000 mm year^{-1} Mean temperature 13°C	Field mapping of the stream networks (from 2 to 4 surveys for each watershed); discharge data available	Four catchments from 2.75 to 5.59 km^2 (except one catchment of 16.97 km^2)	Two rounds in early and late summer, years 2012, 2014, and 2015	

Table 1
Continued

Reference	Location	Climate	Observations	Areal extent	Temporal extent
Ward et al. (2018)*	Headwater mountain catchment in Oregon, USA Mean precipitation 2,302 mm year⁻¹ Mean January temperature 0.6°C Mean July temperature 17.8°C (from Greenland, 1993)	Four field surveys, 15 pressure transducers	0.96 km²	Field surveys from May to August 2016, pressure transducers: 11 months from October 2015	
Yu et al. (2018)*	South-eastern Queensland, Australia Transitional temperate to subtropical	43 stream gauges to mean daily discharge	21.3 km²	1963 (oldest start date for measurements) to 2012 (latest end date)	
C. K. Jensen et al. (2019)*	High-relief headwater catchment in southwest Virginia Mean precipitation over 1,000 mm year⁻¹ Mean January temperature from −4°C to 1°C Mean July temperature from 19°C to 22°C	51 flow intermittency sensors and field measurements	0.33 km²	10 months	
Kaplan et al. (2019)	Various nested subcatchments in the Attert catchment, Luxembourg Influence of oceanic climate Mean annual precipitation about 850 mm year⁻¹ Maximum temperature of 17°C in July and minimum of 0°C in January	Time-lapse imagery, electric conductivity, and stage measurements (182 sites of observations)	28 km² (total catchment area)	Overall, about 4 years from 2013 to 2017	
Van Meerveld et al. (2019)*	Headwater catchment in Switzerland Alpine Mean precipitation 2,300 mm year⁻¹	Three field surveys, streamflow in a neighboring catchment	0.13 km²	October and November 2016 August 2018	
Durighetto et al. (2020)*	Rio Valfredda (Piave river basin), northern Italy Alpine Mean precipitation about 1,500 mm year⁻¹	10 field surveys	5.3 km²	July to early November 2018	
Paillex et al. (2020)*	Val Roseg, Bernina Massif, Swiss Alps Alpine Mean precipitation about 1,000 mm year⁻¹	Modified HOBO sensors for 30 tributary streams	About 28 km² (inferred)	July–November 2017, December 2017 to June 2018	
Perez et al. (2020)	Headwater catchment in the Peri Lagoon, island of Santa Catarina, Brazil Humid subtropical climate Mean precipitation about 1,700 mm year⁻¹ Average temperature varying between 15°C and 27°C	23 overland flow detectors (OFDs) and 11 wells	0.0265 km²	July 2018 to November 2019	

Note. Asterisks marking references in the first column indicate those studies that also attempt to model the network dynamics.

distribution of the active network depends on several topographic and geological features. While Biswal and Marani (2010) linked stream network recession features to morphological characteristics, other authors highlighted the importance of subsurface and groundwater processes for the spatial patterns of flow persistence (e.g., Godsey & Kirchner, 2014; Goulsbra et al., 2014; Kaplan et al., 2020; Shaw, 2016; Ward et al., 2018; Zimmer & McGlynn, 2017). Jaeger et al. (2007) did not find satisfactory area-slope relationships to explain observed channel head locations in forested landscapes in Northwestern USA. In the same vein, Payn et al. (2012) suggested a decreasing influence of topography on stream base flow contributions during the recession. Floriancic et al. (2018) found large differences in flow rates from neighboring slopes with similar geomorphological features, highlighting the importance of bedrock properties and even of debris cover on space-time variability of contributions to low flows.

In the literature, there are many examples of studies that, though acknowledging that topography does not fully explain the observed spatial variability of active river network persistency, use topographic and morphologic indices to model network expansion and contraction. Most of them rely on the mean topographic wetness index (TWI, Beven & Kirkby, 1979), and, to a lesser extent, the topographic position index (TPI, Guisan et al., 1999), which compares the elevation of each cell in a digital terrain model (DTM) to the mean elevation of the neighborhood (González-Ferreras & Barquín, 2017; Jaeger et al., 2019; C. K. Jensen et al., 2018, 2019; Shaw et al., 2017). Existing approaches, however, exploit local morphometric properties of the contributing catchment and operate at the single-grid pixel or river segment level. Therefore, the dynamics of the whole stream network emerge from the aggregation of the local model results through a bottom-up approach. This can induce significant misestimation of the total active length in some circumstances (C. K. Jensen et al., 2018). Moreover, in the existing literature, the effect of stationary topographic and geological characteristics is superimposed on that induced by dynamical hydrometeorological variables, as spatial and temporal patterns of flowing streams are concurrently analyzed via regression models. The influence of topographic and geological attributes on the spatial patterns of flow persistency has not yet been isolated, and the impact of prioritization schemes that involve specific morphometric and geologic characteristics on the ensuing model performance remains unknown.

In this paper, a comprehensive investigation of the recession dynamics of two temporary headwater streams in a Mediterranean watershed is shown. The research consists of the following three main steps: (a) field monitoring and visual inspection of the active (i.e., flowing) stream network, characterized by higher than weekly resolution surveys (average time interval of ∼4–5 days) over a total area of 1.15 km^2, from the end of the 2019 rainy season (i.e., April) until the complete drying up of the channels (June); (b) statistical modeling of the total ADNL by explicitly accounting for the time variability of the hydroclimatic forcing and ET dynamics; and (c) prediction of the spatial distribution of the active nodes based on topographic and geological characteristics of the drainage basin.

The application of the proposed methodology fulfills the following specific objectives: (a) further increasing the range of experimental studies on temporary streams characterizing the effect of seasonal flow recession on the active channels of a headwater catchment with a temperate (hot-summer Mediterranean) climate; (b) providing insights into the time scales of network contraction and seasonal dry down, through an innovative approach relating them dynamically to relevant hydroclimatic variables and evaluating the role of ET in network contraction; and (c) assessing to what extent the spatial distribution of the active river reaches can be explained by a model relying only on topography and evaluating the model improvement with additional information related to the geology.

2. Data and Methods

2.1. Study Area and Geological Setting

The study area consists of two headwater catchments (located approximately at 39.524°N, 16.130°E) feeding the upper course of the Turbolo creek, a tributary of the Crati River in southern Italy (Figure 1a). The Turbolo creek has been investigated for over 20 years (e.g., Mendicino, 1999; Mendicino & Sole, 1997), and streamflow in its upper course is monitored at the outlet of Fitterizzi section, where both a weather station and a water stage gauge are installed, managed by the Regional Agency for the Protection of the Environment (ARPACal).
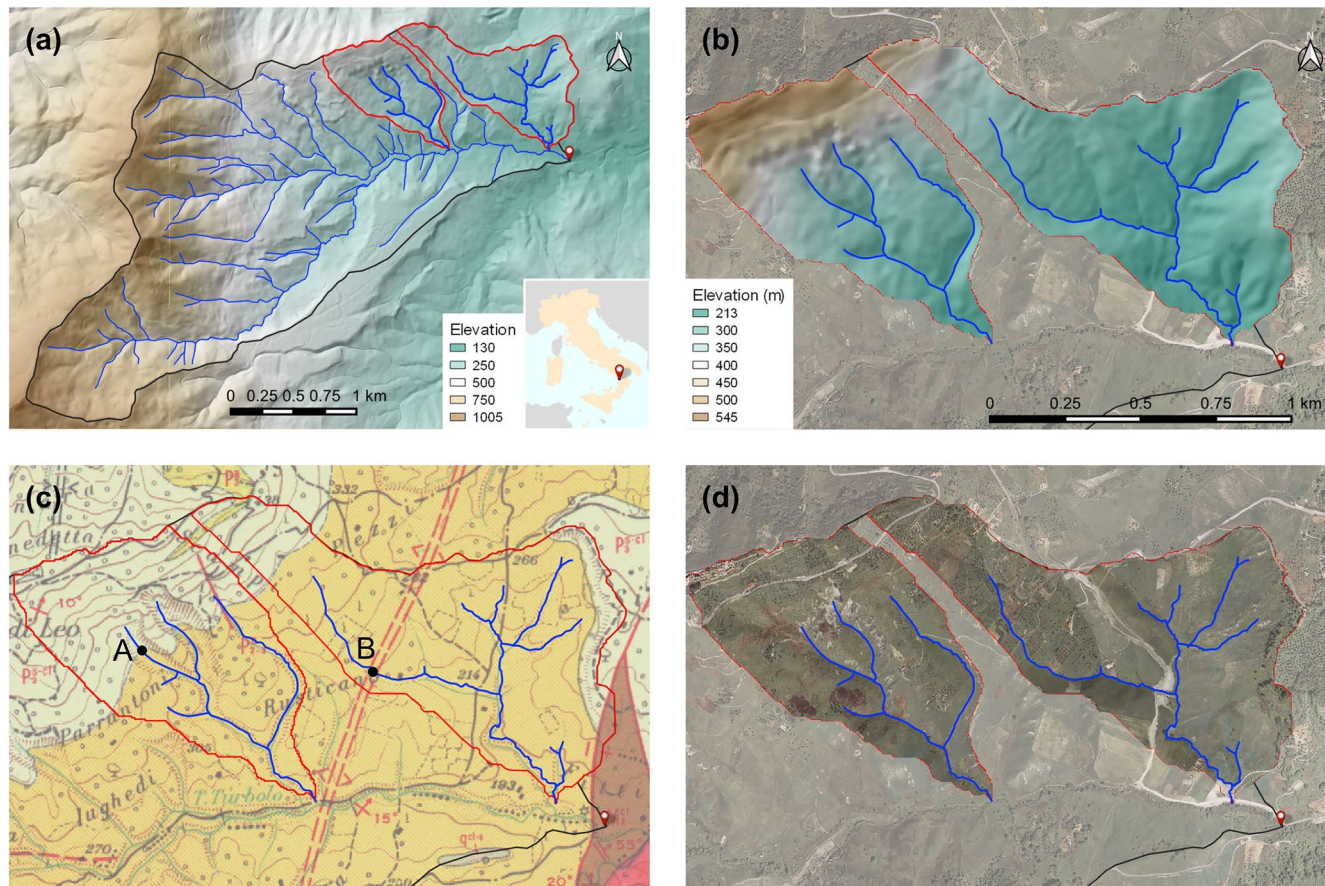
Figure 1. Study area: (a) the upper Turbolo catchment closed at the Fitterizzi outlet (red pin). Red outlines highlight the two study headwater catchments; (b) zoom of the two headwater catchments (W catchment on the left, E catchment on the right); (c) geolithological map of the study area: silty marly clays of the Middle-Late Pliocene are shown in yellow; overlapping Late Pliocene sandy-conglomerate formations are drawn in light beige. The double dashed red line represents the anticline fold. Point A highlights the intersection at the lowest elevation of the separation line between the two sandy and clay lithological formations with the main channel of the W catchment drainage network, point B the intersection of the anticline fold with the E catchment drainage network; (d) study catchments areas and drainage networks overlaid on orthophotos provided by the Calabria Region geoportal.

The upper Turbolo creek catchment is ~7 km², with elevation ranging from 183 to 1,005 m a.s.l. Its channel network mainly consists of two forks, originating from the Calabrian Coastal Range, which is dominated by strongly altered and fractured crystalline-metamorphic rocks that entail widespread slope instability and have overall high permeability (Tortorici et al., 1995). The geology allows ample groundwater recharge and storage that sustains almost perennial flow at the Fitterizzi gauge.

The catchment is characterized by steep slopes on the metamorphic rocks in the west. In the eastern part, where the two test catchments are located, slopes are less steep but affected by water erosion processes, inducing shallow landslides and soil creep.

The two headwater catchments selected for this study, hereafter referred to as east (E) and west (W) catchments (in agreement with their geographical position; Figure 1b), are two subcatchments upstream the Fitterizzi gauge with areas of 0.67 and 0.48 km², respectively; their main topographic and geomorphological features are summarized in Table 2. The dominant lithologies (Figure 1c) are silty marly clays of the Middle-Late Pliocene, with poor erosion resistance and low permeability. North-westerly, poorly consolidated, and highly permeable sandy-conglomerate formations of the Late Pliocene (Calabrian) overlap. The sharp permeability contrast between the two lithologies results in shallow unconfined aquifers that feed temporary springs. The surface layers of the clay formations are generally altered and more permeable than the underlying layers. Moreover, they are characterized by variable thickness due to the aforementioned geomorphological characteristics and because of an anticline fold (Figure 1c). These layers also contain shallow

Table 2
Summary of the Main Properties of the E and W Catchments

$TPI = Z_0 - \sum\limits_{i=1}^{8} Z_i / 8$

	W catchment	E catchment
Catchment area (km²)	0.48	0.67
Maximum elevation (m a.s.l.)	545	481
Mean elevation (m a.s.l.)	358	263
Minimum elevation (m a.s.l.)	213	183
Average exposure	NW	NW
Average slope (°)	23	15
Maximum TWI	14.67	16.21
Mean TWI	4.50	5.13
Maximum TPI	2.80	0.90
TPI standard deviation	0.24	0.16
Minimum TPI	−1.70	−0.93
GDNL (km)	2.26	2.88

Notes. GDNL is the geomorphic drainage network length, TWI the topographic wetness index, and TPI the topographic position index (calculated through the homonymous GDAL—geospatial data abstraction library—algorithm in QGIS). For each cell, $TPI = Z_0 - \sum_{i=1}^{8} Z_i / 8$, where Z_0 is the elevation of the cell under evaluation and Z_i the elevation of each of the eight surrounding cells.

aquifers seasonally contributing to surface flow (more details about geological features of the area are provided in the supporting information, Figure S1).

The erosive processes affecting the two test catchments are mainly dominated by surface flowing water and landslides, which can cause landscape evolution, especially in areas with limited vegetation cover (including agricultural areas). Therefore, the catchment morphology is likely subject to local changes with consequent variations in channel incision and geometry every few years. The W catchment's drainage network is characterized by eroded gullies, steeper morphology, and bare surfaces with evident signs of recurrent landslides. On the other hand, the E catchment has gentler slopes. As a comparison, Table 2 shows that the TPI standard deviation is 0.24 and 0.16 for the W and E catchments, respectively. Another important difference between the study sites concerns land use (Figure 1d). The E catchment is dominated by nonirrigated arable land (66%), while the W catchment by a dense herbaceous cover (53%). Olive groves are almost equally widespread in the two catchments (27% and 23% in the W and E catchment, respectively). More details about land cover in the two catchments are provided in the supporting information (Table S1).

Finally, it is noteworthy that stretches with standing water, due to low infiltration rates and morphological irregularities, are common in the study area. Standing water was not considered part of the active network, yet it facilitates ephemeral stream reactivations (even of a few hours) in the gullies, even following low rainfall amounts. Standing water was differentiated from slow-moving surface water empirically, evaluating the behavior of an injected tracer. Although it was not systematically measured during the field campaign, the length of the network hosting standing water during the initial and intermediate survey period (i.e., April–May) can be roughly estimated in 15%–20% of the active length.

2.2. Hydrometeorological Data Set

The Fitterizzi monitoring station (Figure 1a) is located very close to the two test catchments (∼175 m from the outlet of the E catchment, and ∼2,150 m from the farthest point of the W catchment). The weather data during the 18-year long period from July 2001 to June 2019 reveal a typical Mediterranean climate (Csa, according to Köppen classification; Köppen, 1936), with hot and dry summers (average July temperature of 24.9°C) and wet, not very cold winters (average January temperature of 7.9°C). The average annual precipitation and reference crop ET are 1,245 mm year⁻¹ (only 26% of which falls between April and September) and 1,236 mm year⁻¹, respectively (Figures 2a and 2b). The 1-year period from July 2018 to June 2019 (corresponding to the dry down month in our survey) was less rainy than average (990 mm year⁻¹) and ET was slightly lower than average (1,205 mm year⁻¹). Nevertheless, May 2019, which is the month with the highest number of field surveys in this study, was particularly wet (94.6 mm, the second rainiest May on record).

The total amount of rainfall during the study period (from April 18, 2019 until the end of June 2019) was 101.8 mm, and the corresponding reference ET was 375.4 mm (Figure 2c). During this 74-day period, there were 23 rainy days (precipitation ≥0.2 mm day⁻¹), 18 in May, with the highest intensity of 28.8 mm day⁻¹ on May 6. The average number of consecutive dry days was 6.4, but June was almost completely dry. The limited rainfall in June corresponded to an almost simultaneous sudden increase in temperatures. Specifically, from June 3 to 7, there was an increase of more than 10°C in the maximum daily temperature and ∼8°C in the mean daily temperature.

Correspondingly, the mean reference ET increased from 4.0 ± 0.7 mm day⁻¹ during the period of April 18–June 3 to 6.9 ± 0.6 mm day⁻¹ during the period of June 4–30.
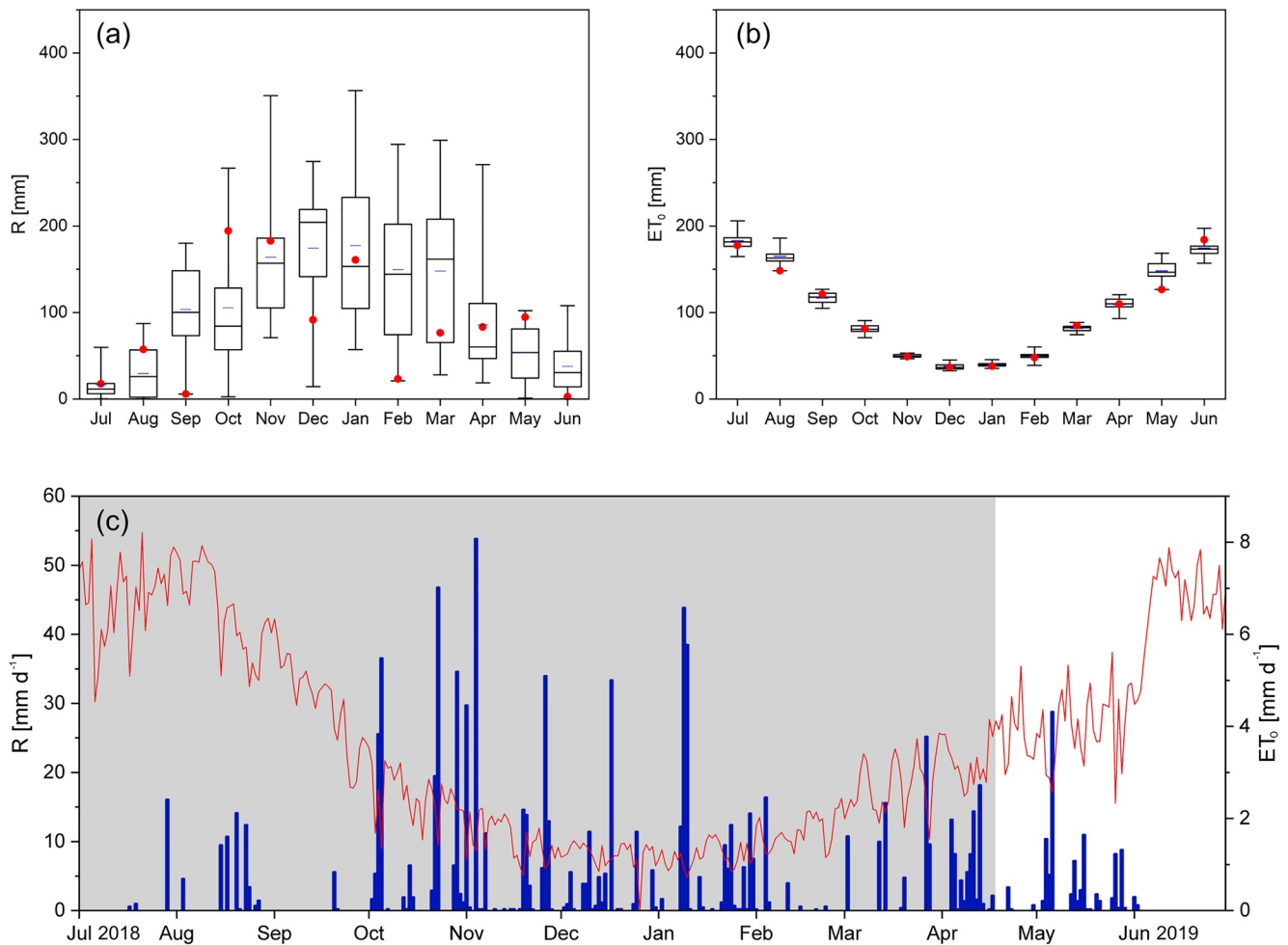
Figure 2. Box plots of (a) accumulated monthly precipitation and (b) reference crop evapotranspiration ET_0 from July 2001 to June 2019. Blue horizontal lines represent the average values, red dots the values in the period July 2018–June 2019; (c) time series of daily precipitation and ET_0 in the period July 2018–June 2019. White background highlights the study period. Note that, while ET_0 in figure (c) was calculated using the Penman-Monteith equation (R. G. Allen et al., 1998), due to the numerous gaps in many variables, the monthly ET_0 in figure (b) was calculated through the Hargreaves-Samani equation following the approach of Mendicino and Senatore (2013b).

Water stage data were also available at Fitterizzi. The stage-discharge rating curve was reconstructed by carrying out frequent discharge measurements (~1 per month) from March to August 2019 with a three-dimensional flow tracker based on acoustic Doppler velocimeter technology, whose sensor allowed reliable measurements starting from flow depths greater than 25 mm, with a maximum tolerance of ±8 mm (more details about the stage-discharge rating curve are provided in the supporting information, Figure S2a).

2.3. Field Surveys and Drainage Network Mapping

The on-site surveys, aimed to reconstruct the topology and dynamics of the flowing network, were carried out from April 2019 until complete dry down occurred in June 2019. The mapping strategy that was replicated was defined by Durighetto et al. (2020) and consisted of hiking the whole stream network, moving upstream along the reaches and collecting the coordinates and status of each network node. A network node is a point along the network where the status (active or dry) has been assessed through on-site surveys. These nodes allow the reconstruction of the spatial and temporal patterns of the flowing network. The GPS coordinates of the nodes were collected with a handheld receiver. The average distance between neighboring nodes was set at 20 m; however, in some cases, adverse morphological and vegetation conditions (especially in the W catchment) did not allow a uniform distance to be maintained throughout the network. The

Table 3
Summary of the Field Surveys

W catchment		E catchment	
Date	ADNL (km)	Date	ADNL (km)
May 18, 2019	1.33	Apr 18, 2019	2.74
May 21, 2019	1.20	May 03, 2019	1.95
May 24, 2019	0.88	May 07, 2019	2.54
Jun 01, 2019	0.87	May 11, 2019	1.95
Jun 05, 2019	0.45	May 17, 2019	2.10
Jun 07, 2019	0.28	May 21, 2019	1.68
Jun 10, 2019	0.14	May 24, 2019	1.62
Jun 15, 2019	0.00	Jun 01, 2019	1.40
		Jun 05, 2019	1.40
		Jun 07, 2019	0.15
		Jun 10, 2019	0.00

Note. ADNL is the active drainage network length.

spatial distribution of nodes is shown in the supporting information, Figure S3. Each node was classified as active when there was flowing water on it and dry otherwise (dry node or node with standing water). The minimum width of flowing water for identifying an active node was fixed to 10 cm. The 10 cm threshold was selected considering different factors. First, this threshold is consistent with the resolutions that other survey techniques can achieve, based, for example, on UAVs and water presence sensors. Furthermore, a width below 10 cm usually is associated with extremely low flows (<0.1 L s^{-1}, approximately). In such conditions, it is not trivial distinguishing surface flow from standing water or saturated soil.

A total of 11 (8) complete surveys were carried out for the E (W) catchment, until the complete dry down of the whole network in both catchments (Table 3). Afterward, periodic (e.g., biweekly) inspections were carried out during the summer season to verify the lack of surface flows in the test catchments (the reactivation of the network took place in November 2019). The overall duration of the campaigns was 53 and 28 days, respectively, for the E and W catchment. For the E catchment, the average time interval between two consecutive surveys was 5.3 days (maximum 15 days, minimum 2 days); for the W catchment, it was 4 days (maximum 8 days, minimum 2 days). The timeline of the surveys was not significantly affected by the underlying weather conditions. Therefore, the surveys were performed under different hydrologic conditions and postponed by 1–2 days only in case of heavy rainfall.

Field recorded information was archived in a GIS environment in which the nodes were connected and the whole network was delineated for each survey. Specifically, the drainage networks were reconstructed from a combination of information derived from field surveys and official sources, such as the DTM and orthophotos provided by the Calabria Region geoportal. The DTM has a spatial resolution of 5 m (enough to reconstruct accurate stream networks; Li & Wong, 2010) and was preliminarily corrected with a pit removal algorithm to eliminate the most evident DTM artifacts (i.e., pits collecting drainage from more than four cells, i.e., 100 m^2), and then flow directions and flow accumulation were calculated through a classical D8-type algorithm (Jenson & Domingue, 1988). The consistency of the flow directions derived from the DTM with the observations was checked by overlaying the tracked nodes. Inconsistencies were solved by manually modifying the DTM, but differences in positions were never greater than two cells (i.e., <10 m). The surveyed nodes were connected by stretches following the GIS-derived flow accumulation grids, and from each grid cell in between two observed nodes, a virtual node was extracted. Each stretch was then set as active only if both the upstream and downstream nodes were observed as active.

Subsequently, for each survey, every node was assigned with an active or nonactive label that made it possible to calculate some global properties, such as the total ADNL (km) and the active drainage density (ADD, km^{-1}). Furthermore, the persistency of active drainage on each stretch *i* during the survey period was

quantified through a persistency index P_i calculated as the ratio of the number of surveys with the stretch classified as active to the total number of surveys (Durighetto et al., 2020).

2.4. Modeling the Drainage Network Length Dynamics

The models used for estimating the total active streamflow network length follow the approach adopted by Durighetto et al. (2020), but some novel elements were introduced to represent the peculiarity of the climate in the study area and the seasonality of the flow regime.

In the first model (model 1, hereafter), the ADNL is assumed to be linearly dependent on the antecedent excess precipitation EP_T (mm) accumulated during the previous T days:

$$ADNL\left(t\right) = k_{EP} \times EP_T\left(t\right) \tag{1}$$

where k_{EP} (km mm^{-1}) is a parameter representing the rate of ADNL increase per unit of EP_T. EP_T is calculated integrating the daily excess precipitation EP (mm day^{-1}) over the period T:

$$EP_T\left(t\right) = \int_{t-T}^{t} EP\left(\tau\right)d\tau \tag{2}$$

where $EP\left(t\right) = R\left(t\right) - ET_C\left(t\right)$, with R (mm day^{-1}) as the daily precipitation and ET_C (mm day^{-1}) as the daily crop ET. The latter can be calculated following R. G. Allen et al. (1998) using a crop coefficient k_c:

$$ET_C = k_c \times ET_0 \tag{3}$$

where ET_0 is the daily reference crop ET estimated with the Fitterizzi monitoring station data from. It is noted that the daily excess precipitation is forced to be positive or null.

The excess precipitation accumulated over the period T in Equation 1 accounts for water either available for direct runoff or stored and released later. The calibration of the model relied on the parameters k_c, k_{EP}, and T, according to the following procedure. First, the parameters k_c and T were estimated by maximizing R^2 by searching in a two-dimensional domain in which physically reasonable ranges of (0, 1) and (0, 60 days) were assumed for k_c and T, respectively. Once the values of k_c and T were fixed, linear regression (which minimizes the sum of squared residuals) was used to estimate k_{EP}. Calibrations were performed for both the E and W catchments, checking their robustness through leave-one-out cross-validations. Furthermore, each study catchment was used for the validation of the model parameters during the calibration in the other catchment.

Model 1 is the only model of the three models proposed by Durighetto et al. (2020) that accounts for evapotranspirative losses. In contrast to the alpine climate where it was first applied, in our study area, the advent of high temperatures, typically from late spring, leads to a significant and rather sudden increase in ET (Figure 2c), making occasional rain showers ineffective for the groundwater recharge. Therefore, the term EP_T tends to zero rather rapidly (depending on T), resulting in the complete dry down of the stream network. Notably, in the calibration strategy shown in this paper, the parameter k_c represents the average behavior of the whole vegetation in the catchment and can implicitly include the effect of water stress conditions; therefore, the accumulated ET_C calculated for the whole analysis period is presumably representative of the accumulated actual ET.

The importance of ET for the contraction and dry down of the Turbolo river network was further evaluated by comparing model 1 to the other two models proposed by Durighetto et al. (2020) in which EP is replaced by precipitation. Specifically, the simplest of these models simply assumes that the ADNL linearly depends on the precipitation R_T (mm) accumulated in the previous T days through a coefficient k_P (km mm^{-1}). It will be called model 2, hereafter:

$$ADNL = k_P \times R_T\left(t\right) \tag{4}$$

The last model (model 3, hereafter) considers two amounts of precipitation (R_{T1} and R_{T2}) as explanatory variables for ADNL, accumulated over different periods T_1 and T_2 to account for different contributions

(interflow and base flow, respectively) to the flow. These two quantities are then linked to ADNL with linear regression using the coefficients k_{P1} and k_{P2}:

$$\text{ADNL} = k_{P1} \times R_{T_1}(t) + k_{P2} \times R_{T_2}(t) \tag{5}$$

Similar to model 1, models 2 and 3 also have no parameters accounting for the length of the permanent drainage network. Therefore, model 2 needs calibration only for parameters k_P and T, while k_{P1}, k_{P2}, T_1, and T_2 are calibrated for model 3. The calibration procedures adopted for these two models are similar to that used with model 1, that is, for each model, the optimal set of parameters was selected by maximizing R^2 with either T or T_1 and T_2 (for further details, the reader is referred to Durighetto et al., 2020). The performance indices considered for model comparisons were the R^2 and the mean absolute error (MAE) between the observed and modeled ADNLs. Furthermore, models were intercompared using the Akaike information criterion (AIC), which combines model performance and complexity. Specifically, the AIC corrected for small sample sizes AIC_c was used (Akaike, 1974):

$$\text{AIC}_c = 2 \frac{n_p + 1}{n_s} + \ln \frac{\text{RSS}}{n_s} + 2 n_p \frac{n_p + 1}{n_s - n_p - 1} \tag{6}$$

where RSS is the residual square sum, n_p the number of calibrated parameters, and n_s the sample size.

Finally, parameter uncertainty of models 1–3 was addressed through a simplified generalized likelihood uncertainty estimation (GLUE) analysis (Beven & Binley, 1992). Specifically, for each model, the set of parameters determining R^2 values greater than 95% of the maximum were selected from the related n-dimensional domains (where n is the number of parameters calibrated for each model). Then, for each parameter, the related posterior marginal probability distribution function (pdf) was derived and compared with the best fit.

2.5. Modeling the Spatial Distribution of the Active Drainage Network

Compared to approaches in the literature that aimed to provide spatially distributed information of the degree of network activity (e.g., González-Ferreras & Barquín, 2017; Jaeger et al., 2019; C. K. Jensen et al., 2018; Kaplan et al., 2020), the novelty of the method proposed here is that it starts from the active drainage network total length (whose extent is estimated based on a moving time window in which the antecedent excess precipitation is dynamically calculated) and then focuses on the allocation of the estimated total length in space, depending on local geomorphological or geological features. The latter step is carried out by transferring the information concerning the nodes surveyed to the grid cells making up the DTM, thus representing the study area through a regular grid with a resolution equal to that of the DTM.

Topographic features can be the foundation of a straightforward and objective method for assessing the spatial distribution of the ADNL. Among the various terrain metrics, the TWI is likely the one that more clearly shows a direct link with runoff persistency (e.g., C. K. Jensen et al., 2018, 2019; Shaw et al., 2017).

If it is assumed that the persistency of surface runoff in a given grid cell is directly dependent on the TWI, then it is possible to spatially distribute the active network across the whole stream network. This can be accomplished by locating it such that it starts from the cell with the highest TWI value and gradually decreases until it reaches a threshold value that corresponds to a network length equal to the (observed or modeled) ADNL. This approach can be pursued once a bijective correspondence between network length and TWI values has been defined. Specifically,

1. if two grid cells are connected horizontally (i.e., in the N-S or E-W directions), the associated length of the channel is equal to the lateral dimension (resolution) of the cell l;
2. if two grid cells are connected diagonally (NW-SE or NE-SW directions), the associated length is equal to $\sqrt{2}\,l$; and
3. in the case of isolated cells, the associated length can be arbitrarily assumed between 0 and $\sqrt{2}\,l$ (in our case, a length equal to $0.5l$ was set).

In some cases, when suggested by either field surveys or geological analyses, the general rule of dependence on higher TWI values can be amended by prioritizing or penalizing reaches that have specific features (e.g.,

the presence of a spring or, conversely, a wide alluvial bed with high storage potential). In particular, if permanent or semipermanent springs are identified, active cells can be allocated primarily downstream of the springs, still following a higher-TWI-based rule that is limited to the downstream channels until the outlet is reached and then moving to the remaining portion of the drainage network. Of course, this approach cannot be separated from an accurate knowledge of the pedolithology and bedrock geology of the study area, where reaches prioritization or penalization is dictated by field surveys or targeted geological investigations.

The accuracy of the model was evaluated through cell-by-cell comparisons involving, for every survey i, all the cells of the geomorphic drainage network. The results were summarized in confusion matrices, from which an accuracy index was achieved:

$$\text{Accuracy}_i = \frac{\text{TP}_i + \text{TN}_i}{n} \tag{7}$$

where TP_i and TN_i represent the cells correctly modeled as active (true positives) and not active (true negative), respectively, and n is the total number of cells belonging to the geomorphic drainage network, that is, the sum of TP_i, TN_i, false positives FP_i (i.e., cells erroneously modeled as active), and false negatives FN_i (i.e., cells erroneously modeled as not active).

3. Results

3.1. Active Drainage Network Observations

Table 3 shows the observed ADNL for the 19 surveys. In the E catchment, the ADNL changed from a maximum of 2.74 km (95% of the potential—geomorphic—drainage network, ADD = 4.09 km^{-1}) to 0 in ∼53 days, with an average observed value of ∼1.59 km. The high initial value of the active network length is most likely due to the precipitation events in the previous 2 weeks (∼80 mm and 13 rainy days out of 14; Figure 2c). Despite a general decreasing trend, the dynamics of the ADNL are nonmonotonic because the rainfall events between May 3 and 7 (45.8 mm overall) and between May 11 and 17 (25 mm overall) led to a temporary increase of the variable. On the other hand, in the W catchment after the first survey (May 18) no relevant rainfall events occurred until the complete dry down (∼28 days later), with an average of less than 1 mm day^{-1} of rainfall; hence, we observed a continuous decrease of ADNL from the first observed value (1.33 km, corresponding to 59% of the geomorphic drainage network, and an ADD = 2.77 km^{-1}) to 0, with an average observed ADNL of ∼0.64 km.

Disconnected ADNL (i.e., the length of the portion of the active drainage network not connected to the outlet) was not common in both catchments. In the E catchment, only during one survey (June 7) was the active network disconnected (5.3% of the geomorphic network length). On the other hand, the rougher morphology of the W catchment led to some disconnected portions of the network in six out of eight surveys, but with disconnected lengths that never exceeded 15% of the geomorphic network.

Figure 3 shows the spatial distribution of the persistency index P_i for the study catchments. Owing to the ephemeral nature of the stream network in this region, the mean persistency values in the E and W catchments are 0.55 and 0.30, respectively. Figure 3 also highlights a significant spatial variability of P throughout the network; in particular, both catchments have one main branch where P_i values are remarkably higher than all the other reaches. This pattern can be reasonably linked to the lithogeological features of the study sites (Section 2.1). Specifically, point A (reported in both Figures 1c and 3) upstream of the most persistent branch in the W catchment represents the lowest elevation where the two sandy and clay lithological formations intersect the main channel, while point B (also drawn in Figures 1c and 3) upstream of the most persistent branch in the E catchment is the approximate location of the intersection of the anticline fold with the drainage network. Both points A and B play an important role because the geological features that correspond to those points foster temporary springs.
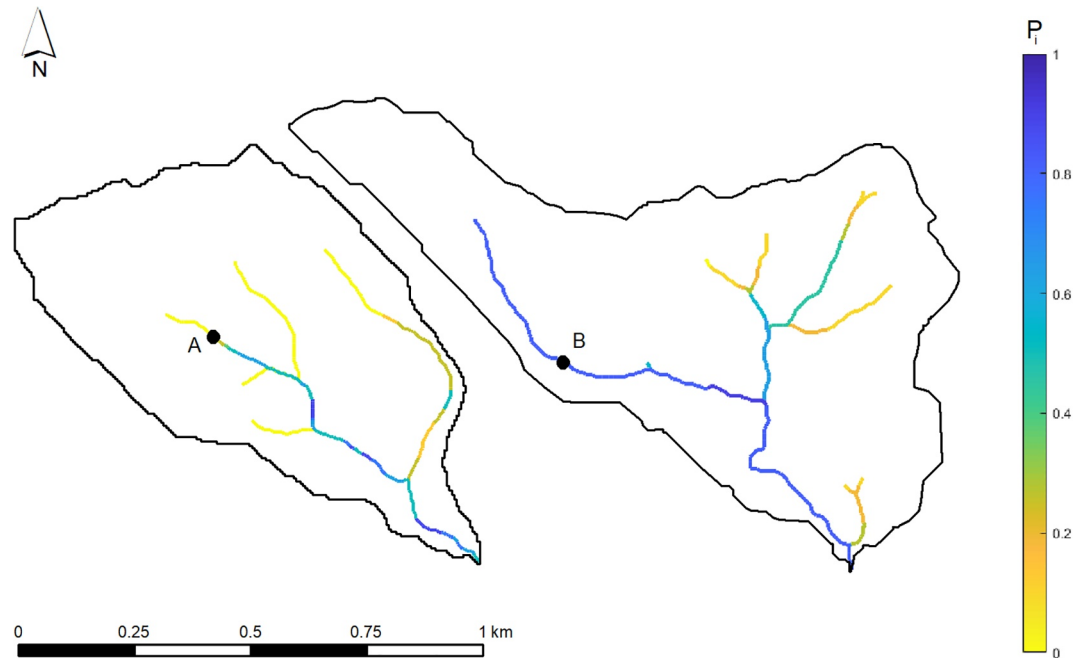
Figure 3. Persistency index P_i for the E and W catchments. Points A and B from Figure 1c are also reported.

3.2. Active Drainage Network Length Modeling

From April 18 to June 30, 2019, a significant decreasing trend in the average daily discharge was recorded, from 104 to 23 L s^{-1}, respectively. The highest average daily discharge (198 L s^{-1}) was recorded after the event that occurred on May 6 (the hydrograph for the whole study period is provided in the supporting information, Figure S2b). Figure 4 relates the ADNLs of the E and W catchments to the average daily discharge Q at the Fitterizzi gauge. The observed discharge is likely too high and shows a reduced variability in time if compared with the actual drainage network length in the study catchments since Q reflects the hydrological processes taking place in a larger area (7 km^2 against 1.15 km^2), including the mountain areas
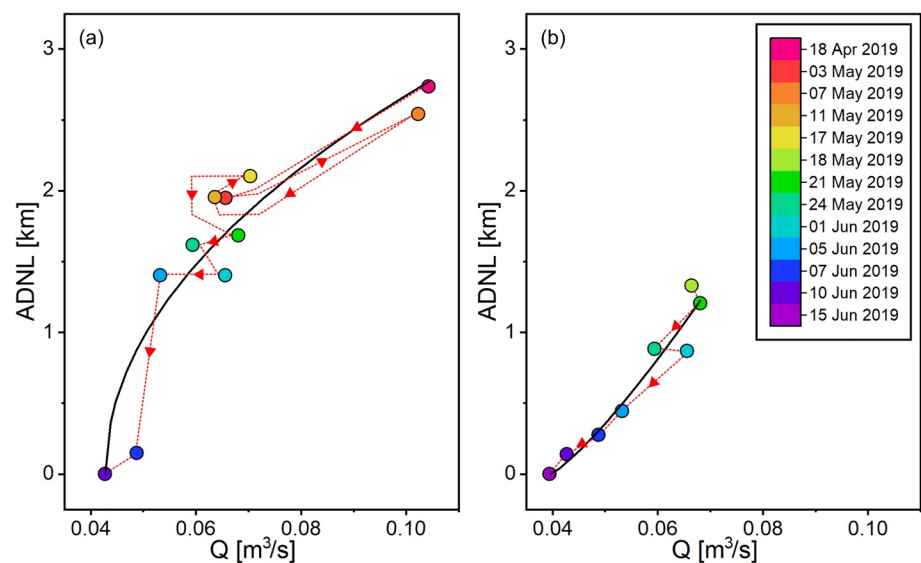

Figure 4. Observed mean daily runoff Q versus active drainage network length (ADNL) observed in (a) the E and (b) the W catchment. Different fill colors highlight the date for each point of the series, while the red dashed tracks indicate the time evolution of observations in the Q-ADNL domain.

Table 4
Comparison of the Calibrated Parameters With Models 1–3 and Related Performance

Model	Parameters (E catchment calibration)	E catchment (calibration) R^2	E catchment (calibration) MAE	W catchment (validation) R^2	W catchment (validation) MAE	Parameters (W catchment calibration)	E catchment (validation) R^2	E catchment (validation) MAE	W catchment (calibration) R^2	W catchment (calibration) MAE
Model 1 Equation 1	$T = 31$	0.92	0.19 ± 0.02	0.83	0.43	$T = 34$	0.79	0.53	0.98	0.05 ± 0.01
	$k_c = 0.449$					$k_c = 0.755$				
	$k_{EP} = 0.034 \pm 0.0006$					$k_{EP} = 0.035 \pm 0.0003$				
Model 2 Equation 4	$T = 24$	0.63	0.42 ± 0.03	0.83	0.70	$T = 9$	0.58	0.58	0.96	0.07 ± 0.01
	$k_P = 0.026 \pm 0.0007$					$k_P = 0.047 \pm 0.0012$				
Model 3 Equation 5	$T_1 = 5$	0.78	0.27 ± 0.02	0.95	0.59	$T_1 = 8$	0.58	0.70	0.99	0.04 ± 0.01
	$T_2 = 24$					$T_2 = 18$				
	$k_{P1} = 0.025 \pm 0.0023$					$k_{P1} = 0.029 \pm 0.0015$				
	$k_{P2} = 0.021 \pm 0.0009$					$k_{P2} = 0.007 \pm 0.0005$				

Notes. The left side of the table refers to the calibration performed in the E catchment, where R^2 and the mean absolute error (MAE) for the W catchment were calculated using the mean values of the parameters k_{EP}, k_P, k_{P1}, and k_{P2}. Analogously, the right side of the table shows the results achieved with the calibration performed in the W catchment. Parameters units: T, T_1, T_2 (days); k_c; k_{EP}, k_P, k_{P1}, and k_{P2} (km mm^{-1}); R^2; MAE (km).

with geolithological characteristics leading to semiperennial flow (Section 2.1). Nevertheless, in both catchments, we tried to express the observed ADNLs as a function of the observed discharge as

$$\text{ADNL} = \alpha \left(Q - Q_0 \right)^\beta \tag{8}$$

where α is a constant, β is the scaling exponent, and Q_0 is the highest discharge value for which ADNL = 0. Calibration led to a value of 0.494 for the scaling exponent value in the E catchment, which is within the literature range (Godsey & Kirchner, 2014; C. Jensen et al., 2017). Instead, in the W catchment, it is >1 (Figure 4b). This difference in the exponents is possibly generated by the difference in the dates when the surveys started (in the W catchment, the surveys started closer to the dry down than in the E catchment).

The power regressions based on Equation 7 were well correlated to observed ADNLs (R^2 equal to 0.87 and 0.94, MAE equal to 0.23 and 0.08 km, respectively, for the E and W catchment). Nevertheless, they oversimplify the different response times of different hydrological processes (i.e., active network expansion and contraction and discharge generation and routing) triggered by meteorological forcing, enhancing the risk of spurious correlations. In Figures 4a and 4b, the colors of the circles and the red dashed tracks highlight the time evolution of observed points in the Q-ADNL domain. In the E catchment, we observed some counterclockwise hysteretic effect, similar to those described by Zimmer and McGlynn (2017) during the precipitation event that took place on May 6, 2019. The ADNL was slightly lower during the rising limb than during the receding limb (ADNL = 1.948 km and Q = 66 L s^{-1} on May 3, ADNL = 1.953 km and Q = 64 L s^{-1} on May 11), confirming that network contraction might have a delayed response compared to flow recession. Other examples in support of this finding exist. For instance, in the E catchment, despite a flow recession of ~12 L s^{-1} from June 1 to 5 (with 2.8 mm of rainfall in-between), ADNL did not vary. The counterclockwise hysteretic effect emerges despite that the size of the catchments where the ADNL was monitored (1.15 km^2 altogether) is much smaller than the contributing area at the discharge gauging station (7 km^2). Instead, such an instance is expected to smooth the discharge response and hasten the ADNL response.

Drainage network dynamics were related to the underlying meteorological drivers (precipitation and ET) using the statistical models described in Section 2.4. Table 4 summarizes the results achieved using model 1 that accounts for ET, and its performance is compared to models 2 and 3 that only rely on precipitation data. It shows that model 1 systematically outperforms other models in the E catchment with a longer survey period, while in the W catchment, with a shorter survey period, statistics are comparable. The decrease of performance observed in the E catchment when ET is not included in the statistical regression (models 2 and 3) indicates that in Mediterranean climates, ET plays a relevant role for drainage network dynamics.

Nevertheless, due to the simplicity of the models, the AIC-based analysis performed heavily penalized models with a larger number of parameters. In the E catchment, the AIC_c values of the models 1, 2, and 3 were 4.7, 2.8, and 11.2, respectively. In the W catchment, they were instead 9.2, 2.3, and 25.6. According to the AIC ranking, model 3 is by far the less performing in all cases. In the E catchment, differences between models 1 and 2 are not so sharp (ΔAIC_c lower than 2) indicating comparable performance according to Burnham and Anderson (2002). As expected, in the W catchment owing to the reduced number of observations, model 2 clearly outperforms the others. Overall, the results based on both statistical performance indices and AIC suggest that including ET data allows more robust estimates of the flowing length, but precipitation data alone can contribute as a first approximation to evaluate flowing network dynamics even in hot-summer Mediterranean climate.

Focusing on model 1 including ET, we observed some differences in the calibrated parameters between the E and W catchments. The period T over which the excess precipitation was accumulated on the E catchment was slightly shorter than for the W catchment (31 vs. 34 days). This result can be explained by the smoother landscape of the E catchment compared to the W catchment, where incised channels might more strongly connect the surface drainage network to the subsurface flow. However, this hypothesis needs to be further verified, given the uncertainty in the estimate of T in the W catchment (see Figure 6 and the related uncertainty analysis). The calibrated k_c value in the E catchment was also lower than the optimal k_c in the W catchment (0.449 vs. 0.755), in line with the observed differences in the land use of the two catchments (with more agriculture and controlled vegetation growth in the E catchment). The patterns of the R^2 values in the T-k_c domain for both the E and the W catchments are shown in Figures 5a and 5b, respectively. Even though R^2 values tend to be higher in the W catchment, which can be simulated more "easily," the patterns are quite similar in the two cases. In particular, the smallest T values are associated with the lowest R^2 values for any k_c, suggesting that the short-term cumulative value of weather variables is poorly correlated with the observed dynamics of the drainage network.

The T and k_c parameters summarize the effects of the differences in topography and land cover in the two catchments. Taking this into account, interestingly, the ratio between the ADNL and the accumulated excess precipitation is almost the same (0.034 ± 0.0006 and 0.035 ± 0.0003 for the E and W catchment, respectively). Table 4 also shows the cross-validation analysis performed for the parameter k_{EP}. The results highlighted the robustness of the model (coefficients of variation of k_{EP} on the order of 0.01) that was also confirmed by the MAE values achieved with different parameter subsets.

Figures 5d and 5e show the modeled network dynamics using the parameter sets calibrated with both the test catchments and the observations. The graphs provide a visual representation of the good performance of the models that are confirmed by the high R^2 and low MAE values (Table 4). Model 1 not only performs very well in the catchment where it is calibrated ($R^2 = 0.92$ and 0.98, MAE $= 0.19 \pm 0.02$ km and 0.05 ± 0.01 km, for the E and W catchments, respectively) but also provides reliable forecasts in the corresponding validation catchments ($R^2 = 0.83$ and MAE $= 0.43$ km in the W catchment; $R^2 = 0.79$ and MAE $= 0.53$ km in the E catchment).

Figures 5a and 5b show that, for the E catchment, the best set of parameters is mostly concentrated in a well-defined region of the T-k_c domain, while for the W catchment the region of the parameter space where performances are higher is more scattered. Uncertainty analysis performed through the GLUE approach confirmed this behavior. For both the catchments, Figure 6 isolates the marginal probability density functions (pdfs) of the parameters T and k_c whose combination allowed us to achieve R^2 values greater than 95% of the maximum (the pdfs of the parameter k_{EP} are also shown in the figure for the sake of completeness). In the E catchment, the best fit parameters match the medians of the distributions, highlighting the robustness of the parameterization. On the other hand, the posterior pdfs for the W catchment reveal that a relatively wide range of parameters could provide performances similar to the best fit. This result is most probably due to the shorter duration of the observation period in the W catchment. Despite the relevant uncertainty of the parameters T and k_c (standard deviations of 13.6 days and 0.191, respectively for T and k_c), their posterior medians (45.5 days and 0.643, respectively) are both higher than those found for the E catchment, therefore supporting the previous hypotheses about parameter differences in the two catchments.
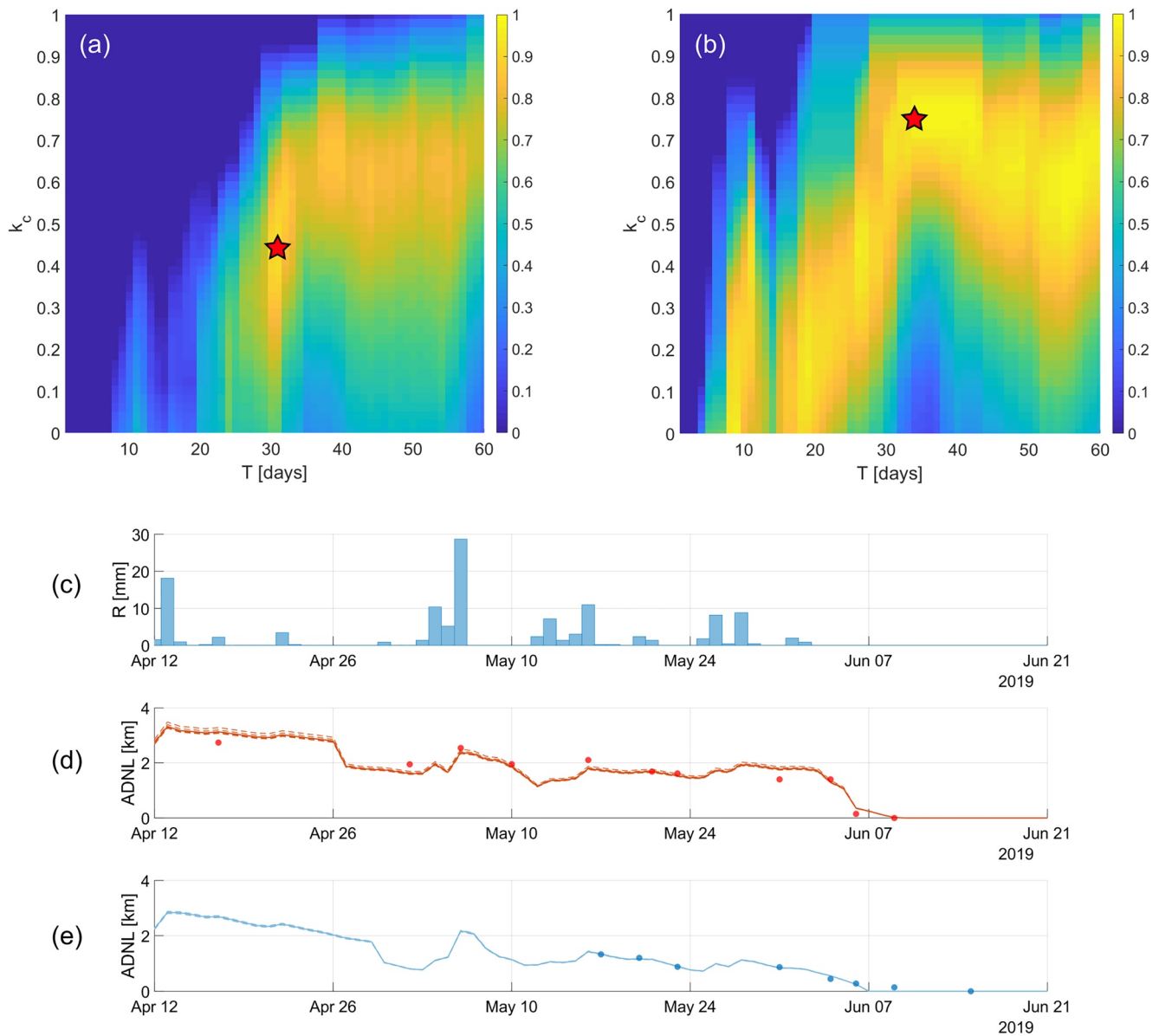
Figure 5. R^2 of model 1 as a function of T and k_c, calibrated for the observations (a) in the E catchment and (b) in the W catchment; (c) daily precipitation during the period from April 12 to June 21, 2019; (d) calibrated model based on model 1 in the E catchment (red points represent the observed active drainage network length [ADNL] values); (e) calibrated model based on model 1 in the W catchment (blue points represent the observed ADNL values). In (a and b), the red stars highlight the best parameter set. In (d and e), the dashed lines represent the cross-validation results achieved using the calibrated parameter sets.

3.3. Spatial Distribution of the Active Drainage Network

Figure 7 shows the variation of the active network length, considering as active only the cells of the DTM having TWI values equal to or greater than a given threshold. To facilitate the comparison between the two catchments, the active network length and the TWI values were scaled with the catchment area (ADD) and the maximum TWI value (TWI$_{max}$), respectively. The graph highlights an almost linear increase in ADD while reducing the TWI threshold in the W catchment; in the E catchment, instead, the increase in ADD is slower for higher TWI values (i.e., at lower elevations) and faster for lower values. Figure 7 resembles the right tails of TWI frequency distributions in the study catchments (corresponding to the channelized network). Moreover, the observed pattern of ADD versus TWI/TWI$_{max}$ in the E catchment reflects the higher bifurcation ratio of the upstream network, and the presence of a single relatively long main channel in the
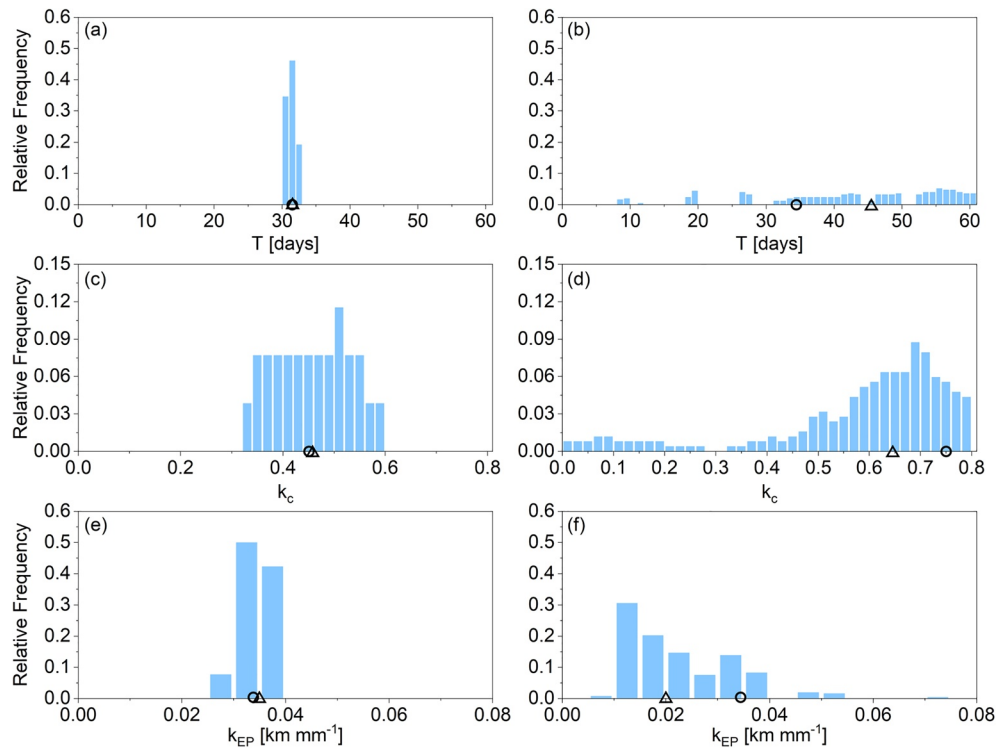
Figure 6. Probability distribution functions of the parameters allowing R^2 values greater than 95% of the maximum for both the E catchment (panels a, c, and e) and the W catchment (panels b, d, and f). In each panel, the circles indicate the best fit (Table 4), the triangles the median value of the pdf.
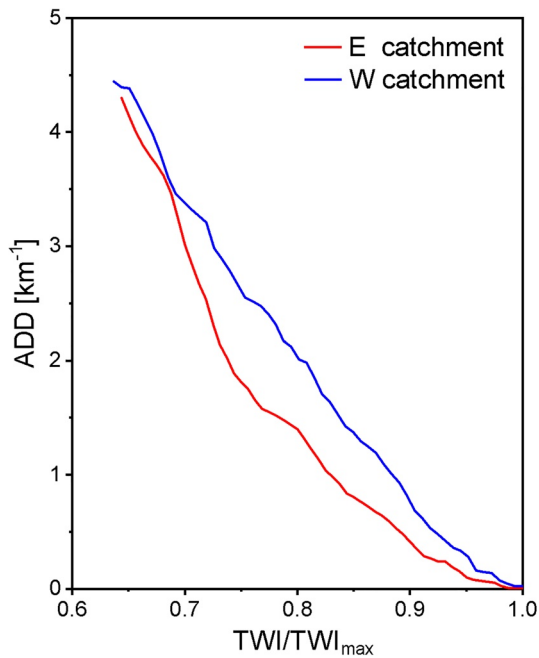

Figure 7. Relationship between the active drainage density (ADD) obtained when only the cells of the digital terrain model (DTM) having the ratio topographic wetness index (TWI)/TWI$_{max}$ equal to or greater than a given threshold are activated and the respective TWI/TWI$_{max}$ thresholds.

lower part of the basin. Therefore, in the E catchment, the ADNL is more sensitive to changes in the TWI threshold for lower TWI values and vice versa.

The TWI-ADNL relationship can be used for modeling the spatial distribution of the active network if TWI values of the cells are significantly correlated with the corresponding persistency values. Specifically, it can be hypothesized that a cell in the channel network with higher TWI is active for longer than a cell with a smaller TWI; hence, its persistency P_i is higher. Indirectly, this assumption implies that the activation of the reaches in the whole network follows a hierarchical order since TWI is a time-invariant feature.

TWI values in the cells that host the geomorphic channel networks are well correlated with P_i (Figure 8) both in the E catchment ($r = 0.714$, $p \ll 0.001$) and the W catchment ($r = 0.833$, $p \ll 0.001$). Correlation analysis suggests that other topographic indices such as TPI, which proved to be useful in other contexts (e.g., C. K. Jensen et al., 2018), cannot add significant information in this case ($r = 0.059$ and 0.098, for the E and W catchments, respectively).

The ADNL-TWI relationships found in the two test catchments were used to drive the spatial distribution of the modeled ADNL in the cells of the DTM. Figures 9a and 9b (left histogram series, labeled with "T") summarize the performance of the whole modeling chain (i.e., ADNL modeling based on effective rainfall and consequent spatial allocation of the channelized sites), highlighting for each survey in each catchment, the percentage of TP, TN, FP, and FN (these results are also provided in
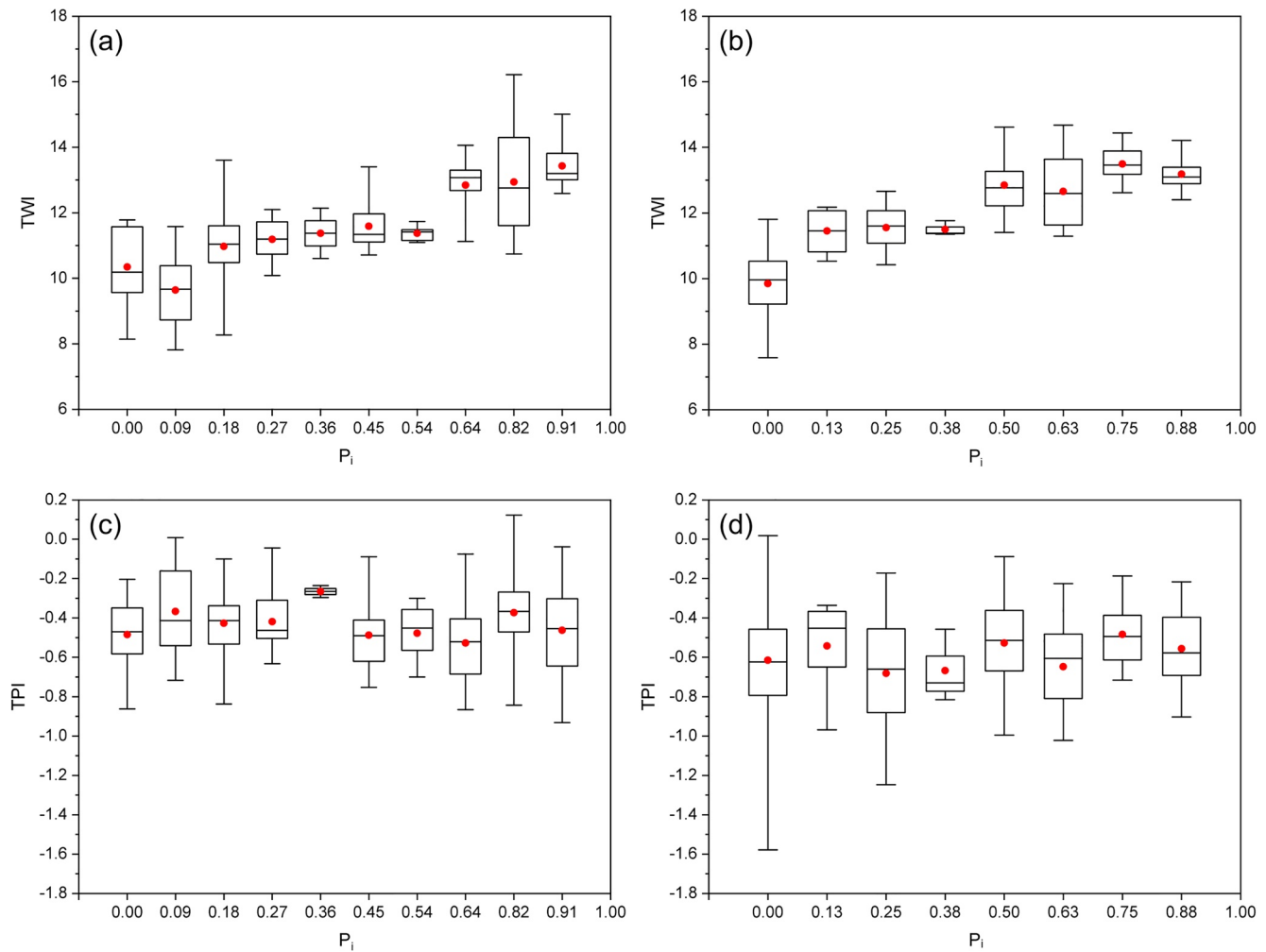
Figure 8. Box plots of topographic wetness index distribution (a) in the E catchment and (b) in the W catchment, and topographic wetness index distribution (c) in the E catchment and (d) in the W catchment, divided according to the corresponding P_i values, for each digital terrain model cell belonging to the geomorphic drainage network. Red dots represent the mean values.

Table S2, as supporting information). The mean accuracy in the E catchment (Figure 9a) varies from 72.8% (June 1) to 99.4% (June 10), with an average value of 81.7%. In the W catchment (Figure 9b), the accuracy varies from 84.8% (June 7) to 97.6% (June 15), with an average value of 89.5%. FP and FN percentages are comparable in both catchments (FP = 7.8% and FN = 10.5% in the E catchment, FP = 4.2% and FN = 6.3% in the W catchment), highlighting the similar model performance in the two case studies.

A comparison of the modeled spatial distribution of the active cells with the observational data (some examples representative of different wetness conditions are given in Figure 10) highlights that model performance can be further improved integrating the topographical features summarized by the TWI with lithogeological information. Specifically, the stream reaches starting from points A (sand-clay interface, Figure 1c) and B (anticline) where temporary springs emerge (Section 3.1) need to be prioritized when defining the activation rules since observations showed that cells belonging to such reaches are more quickly activated than cells with higher TWI values belonging to other reaches. Therefore, the spatial allocation of the active cells in each catchment is ruled by two TWI-ADNL curves, with the second (low priority) activated only when the maximum ADNL associated with the first (high priority—reaches starting from point A or B) is reached.

Assuming the priorities suggested by the analysis of the lithogeological features, the results shown in Figures 9a and 9b (right histogram series, labeled with "T-G") were achieved. The mean accuracy in the E
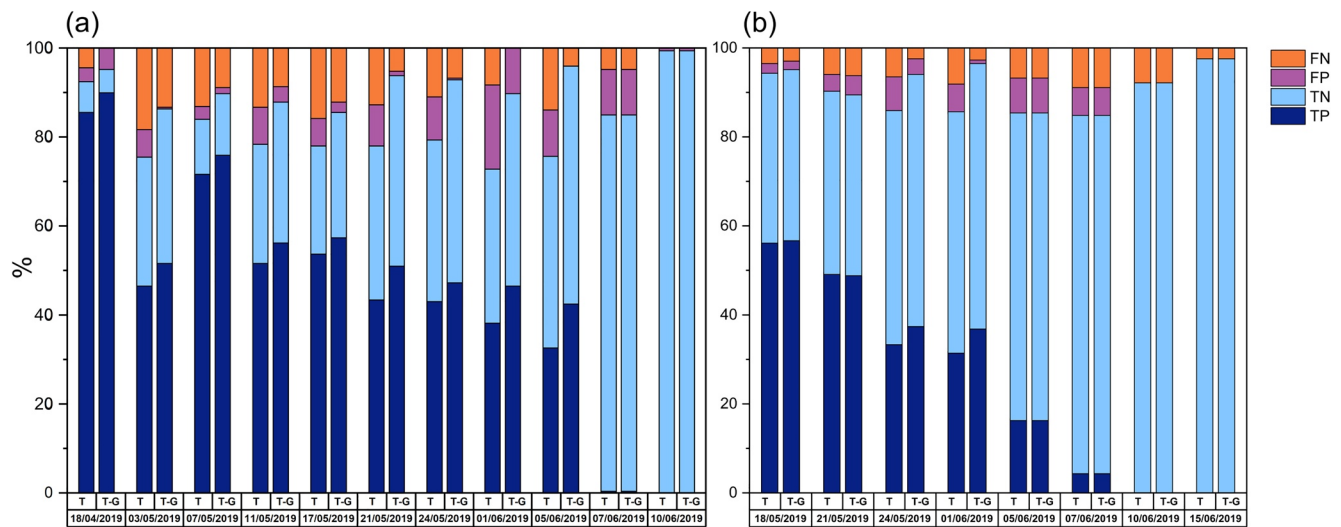
Figure 9. Summary of cell-by-cell comparison of the observed and modeled spatial distribution of active cells for all surveys: (a) E catchment and (b) W catchment. In each graph, the left histogram series are related to the model using only topographic wetness index (TWI) (label "T"), the right histogram series to the model using both TWI and lithogeological information (label "T-G"). TP, true positives; TN, true negatives; FP, false positives; FN, false negatives.

catchment increases by 9.4% compared to the model relying only on TWI (Figure 9a), with an average value of 91.1% and a range that varies from 84.9% (June 7) to 99.4% (June 10). In the W catchment (Figure 9b), the improved version of the model increases model performances to a lesser extent (+2.4%). FP and FN percentages remain comparable in both catchments, but with smaller values compared to the version of the model that uses only topographic information (FP = 3.2% and FN = 5.8% in the E catchment; FP = 3.1% and FN = 5.0% in the W catchment).

Figure 10 shows some examples of the cell-by-cell comparisons between observed and modeled active drainage networks using both the TWI-based model and the integrated topographical and lithogeological model. Specifically, for the E catchment, the surveys performed on May 7 and June 5 were selected as representative
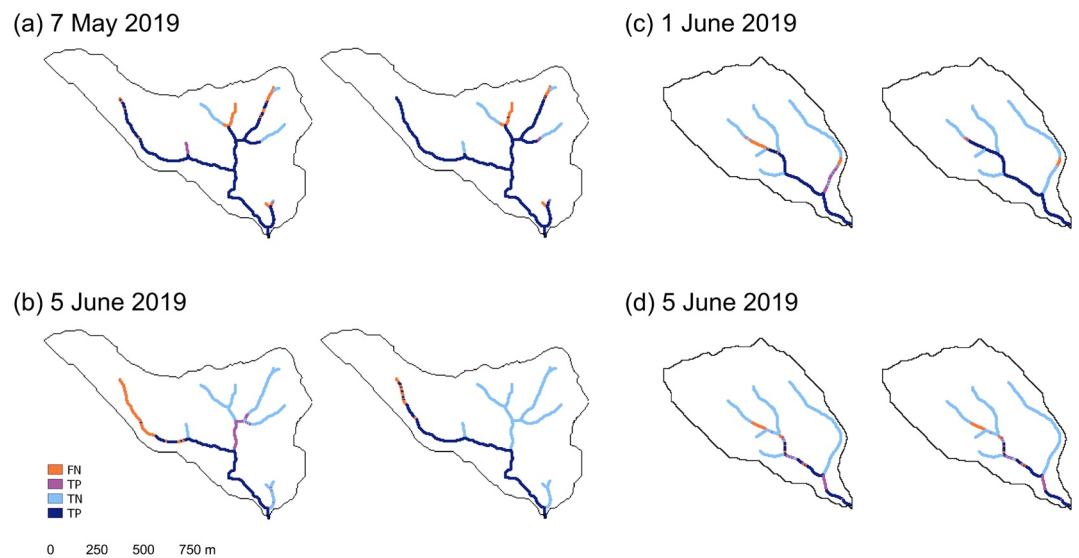

Figure 10. Cell-by-cell comparison of the observed and modeled spatial distribution of active cells: (a) E catchment, May 7, 2019; (b) E catchment, June 5, 2019; (c) W catchment, June 1, 2019; and (d) W catchment, June 5, 2019. For each figure in the panel, the left map is related to the model using only topographic wetness index (TWI), the right map to the model using both TWI and lithogeological information. TP, true positives; TN, true negatives; FP, false positives; FN, false negatives.

of wet and dry (but without complete dry down) conditions, respectively. On the first date (Figure 10a), the catchment was quite wet and the prioritization of the stretch intersecting the anticline had a small effect on the observed spatial pattern of the active network. On the other hand, on June 5 (Figure 10b), the same strategy led to an improvement in the total accuracy of more than 20%. Concerning the W catchment, the example reported in Figure 10c, which refers to June 1, highlights the beneficial consequences implied by the prioritization of the main channel (with an improvement in the accuracy of almost 11%); however, when the main channel is not fully active (June 5, Figure 10d), the two approaches are almost equivalent.

4. Discussion and Conclusions

This study presents the results of a comprehensive analysis based on a field campaign in two Mediterranean catchments in which the active network was monitored during the flow recession phase at the beginning of the summer of 2019 until complete dry down. The paper also presents an integrated model of the space-time dynamics of the active drainage network that couples meteorological, topographic, and geological information in a sequential manner. The temperate Mediterranean climate of the study area (typically characterized by hot and dry summers with high values of potential ET) jointly with the specific focus on network dry down represents one of the key novelties of this work. The work expands the range of hydroclimatic settings within which empirical information on the temporal dynamics of the actively flowing streams is available.

The results shown in this paper strengthen the hypothesis that the temporal variability of the overall active network length is modulated by weather dynamics. Specifically, the high correlation between the antecedent excess precipitation and the active network length suggests the following major conclusions: (a) ADNL temporal variability can be successfully described based on weather data; (b) in the analyzed meteorological setting, there is enough statistical evidence that ET likely improves the prediction of the observed dynamics of the active streams. This outcome allows a step forward from the study of Durighetto et al. (2020), who could not appreciate a visible effect of ET on the temporal dynamics of the flowing length because of the wetness of the underlying climatic conditions (annual precipitation of 1,500 mm, with a mean annual temperature of ∼5°C). The uncertainty on the role of ET modulation highlighted by the AIC_c tests will be reduced with further research into how different hydrological processes control the dynamics of the active length; (c) while the temporal dynamics of the ADNL are controlled by the underlying climatic variability, the actual length of active streams also depends on topographic or geological features, which in model 1, influence the period of integration T over which the accumulated excess precipitation needs to be evaluated. Specifically, T turns out to be longer in the more incised but smaller W catchment, and shorter in the gentler E catchment. Provided that differences in land cover (which modulates ET) and topography are summarized by the different values of the parameters k_c (Equation 3) and T (Equation 1), the proportionality factor between accumulated excess precipitation and ADNL (i.e., ≈0.035 km mm^{-1}) was almost the same for the two neighboring study catchments, despite the differences in catchment area and geomorphic drainage density.

The statistical model linking active length and antecedent excess precipitation was compared to an alternative approach that relies on a power function linking ADNL and discharge. Our results indicate (Section active drainage.2) a good performance of the discharge power function (Equation 8) in describing ADNL dynamics, though the performance was slightly lower than that of model 1. Discharge is a variable well representing ADNL behavior during the recession phase. Several studies used antecedent discharge to predict recession coefficients (e.g., Bart & Hope, 2014; Biswal & Nagesh Kumar, 2014; Reddyvaraprasad et al., 2020). However, we argue that relying on weather variables rather than water discharge for modeling ADNL dynamics is preferable for three reasons, other than the performance:

1. Discharge and active network length are two different types of responses to a common hydrological forcing, even though these responses are characterized by distinct characteristic lag-times. This feature is highlighted by the counterclockwise hysteretic behavior observed between Q and ADNL (Shaw, 2016; Zimmer & McGlynn, 2017), which implies that the discharge response is faster than the active network length.
2. In many settings, discharge data are much rarer and much more challenging to gather than weather data. Nonetheless, they can be crucial for analyzing the coevolution of ADNL and Q and for characterizing

the hysteresis in the stream length-streamflow relationship. Therefore, a larger availability of streamflow data is certainly desirable.

3. The use of meteorological data makes the parameters of the regression less sensitive to the specific observation period during which the survey was carried out. As an example, Table 4 shows that model 1 calibrated in the W catchment (less field surveys and only during the last part of the recession period) provides reasonable results also in the E catchment (more field surveys on a slightly longer period), while the power function calibrated in the same period in the W catchment with the scaling exponent greater than 1 is not applicable for the E catchment.

While the weather forcing controls the observed temporal changes in the active network length, the main drivers of the active network's spatial patterns are represented by physiographic features such as topography, hydraulic properties of surface soil, bedrock structure, and permeability, and geological singularities such as faults and anticlines in line with previous studies (Costigan et al., 2016; Godsey & Kirchner, 2014; Goulsbra et al., 2014; C. K. Jensen et al., 2018, 2019; Kaplan et al., 2020; Prancevic & Kirchner, 2019; Whiting & Godsey, 2016). Specifically, the high correlation between the persistency index P_i and TWI for both catchments, which is here enhanced by the spatial homogeneity of soil properties, confirms the primary importance of surface topography in delineating spatial patterns of active drainage networks (C. K. Jensen et al., 2018).

The relatively low number of disconnections observed in the study sites can be explained by the prevalence of clay soils that do not promote the formation of losing streams and water reinfiltration. Nevertheless, even in a rather homogenous geological setting such as the study area (Figure 2c), topography cannot fully explain the spatial dynamics of stream expansion and contraction (C. K. Jensen et al., 2019). The presence of pedological and lithogeological singularities can impair the hypothesis that the location of flowing streams is only constrained by topography (e.g., Godsey & Kirchner, 2014), especially during the recession phase (Payn et al., 2012) and even in neighboring catchments with similar geomorphological characteristics (Floriancic et al., 2018). In our case study, accounting for some key geological features (namely, the sand-clay interface and the anticline) helped to improve the representation of the spatial patterns of active stream dynamics, especially during the late stages of the dry down, when the effect of geological singularities became more evident.

The proposed approach based on a bijective correspondence between the network length and TWI (either with or without prioritization) was shown to be effective in both the case studies investigated herein. As per the aim of the study, a double advance was achieved: first, a statistical framework which provides information about the total active network length (i.e., the model proposed by Durighetto et al., 2020) was successfully integrated with a morphometric model for the identification of the spatial patterns of flowing channels; second, the role of topographic and geological attributes on the spatial patterns of the active network was disentangled from that of hydrometeorological factors.

In general, the concept of prioritization proposed in this work can be made more complicated; for example, the priority given to the stretches located downstream of a geological singularity can be effective only within a given region of influence, for example, as defined by a certain TWI (lower) threshold. However, the adoption of this strategy is conditioned by detailed knowledge of the specific features of the catchment and can be difficult to generalize. Also, the calibration of the statistical model showed that even neighbor subcatchments are described by different sets of parameters. Therefore, information transfer to other networks and generalization of the results is not straightforward and requires adequate knowledge of the new study area, acquired also through several field surveys. Nevertheless, the simple and flexible methodology proposed in this study, including both monitoring and modeling, can be generalized to all headwater flowing networks.

Concerning the burden of the monitoring campaign, it is worth noting that both morphologic and geolithological characteristics are time-invariant features of the catchment. The dependence of the persistency on such features evidenced by our data supports the hypothesis of the existence of a predefined hierarchical order in the activation and deactivation of stretches, implying that those activating later are the first that dry down and vice versa. The consequences of such behavior, which needs to be confirmed and generalized by further studies, are discussed in Botter and Durighetto (2020). These include more straightforward monitoring campaigns of river networks dynamics (in which the activity of less persistent nodes can be inferred

by monitoring more persistent ones), and the possibility of linking the total length of the active network to the spatial patterns of the active streams, as proposed also in this work.

Future work will expand the analysis of the network dynamics in the study area to other recession periods to further validate the model and to confirm the extent of the integration period of antecedent meteorology. Furthermore, the analysis will move beyond the recession phase, including the winter reactivation phase. As suggested by previous studies (e.g., Zimmer & McGlynn, 2018), the expansion and contraction of the flowing network are connected to the seasonal variations of the storage in the underlying shallow unconfined aquifers. Given the peculiar geological features of the area, the temporary springs are likely reactivated only when the water table elevation exceeds a given threshold. This hypothesis will be evaluated in future studies that also use a higher-resolution DTM derived from a LiDAR survey, UAV-based monitoring, and more detailed information about soil properties and bedrock structure.

Data Availability Statement

Weather data are delivered, upon request, by the "Centro Funzionale Multirischi-ARPACAL" (http://www.cfd.calabria.it/). The original DTM, the geolithological map of the study area, and the orthophotos are provided by the Calabria Region geoportal: http://geoportale.regione.calabria.it/opendata. The modified DTM and the experimental data collected for this study are available at Senatore et al. (2020).

References

Abbott, B. W., Baranov, V., Mendoza-Lera, C., Nikolakopoulou, M., Harjung, A., Kolbe, T., et al. (2016). Using multi-tracer inference to move beyond single-catchment ecohydrology. *Earth-Science Reviews*, *160*, 19–42. https://doi.org/10.1016/j.earscirev.2016.06.014

Acuña, V., Datry, T., Marshall, J., Barceló, D., Dahm, C. N., Ginebreda, A., et al. (2014). Why should we care about temporary waterways? *Science*, *343*(6175), 1080–1081. https://doi.org/10.1126/science.1246666

Ågren, A. M., Lidberg, W., & Ring, E. (2015). Mapping temporal dynamics in a forest stream network—Implications for riparian forest management. *Forests*, *6*(9), 2982–3001. https://doi.org/10.3390/f6092982

Akaike, H. (1974). A new look at the statistical model identification. *Transactions on Automatic Control*, *19*, 716–723. https://doi.org/10.1109/TAC.1974.1100705

Allen, G. H., Pavelsky, T. M., Barefoot, E. A., Lamb, M. P., Butman, D., Tashie, A., & Gleason, C. J. (2018). Similarity of stream width distributions across headwater systems. *Nature Communications*, *9*, 610. https://doi.org/10.1038/s41467-018-02991-w

Allen, R. G., Pereira, L. S., Raes, D., & Smith, M. (1998). *Crop evapotranspiration—Guidelines for computing crop water requirements—FAO irrigation and drainage paper 56* (300(9), D05109). FAO. Retrieved from http://www.scscourt.org/complexcivil/105CV049053/volume3/172618e_5xAGWAx8.pdf

Anderson, M. G., & Burt, T. P. (1978). Analysis of spatial water quality and stream networks in the southern Cotswolds during and after the drought of 1976. *Earth Surface Processes*, *3*(1), 59–69. https://doi.org/10.1002/esp.3290030106

Assendelft, R. S., & van Meerveld, H. J. (2019). A low-cost, multi-sensor system to monitor temporary stream dynamics in mountainous headwater catchments. *Sensors*, *19*(21), 4645. https://doi.org/10.3390/s19214645

Bart, R., & Hope, A. (2014). Inter-seasonal variability in baseflow recession rates: The role of aquifer antecedent storage in central California watersheds. *Journal of Hydrology*, *519*, 205–213. https://doi.org/10.1016/j.jhydrol.2014.07.020

Berger, E., Haase, P., Kuemmerlen, M., Leps, M., Schaefer, R., & Sundermann, A. (2017). Water quality variables and pollution sources shaping stream macroinvertebrate communities. *Science of the Total Environment*, *587*, 1–10. https://doi.org/10.1016/j.scitotenv.2017.02.031

Beven, K. J., & Binley, A. (1992). The future of distributed models: Model calibration and uncertainty prediction. *Hydrological Processes*, *6*, 279–298. https://doi.org/10.1002/hyp.3360060305

Beven, K. J., & Kirkby, M. J. (1979). A physically based, variable contributing area model of basin hydrology [Un modèle à base physique de zone d'appel variable de l'hydrologie du bassin versant]. *Hydrological Sciences Journal*, *24*(1), 43–69. https://doi.org/10.1080/02626667909491834

Biswal, B., & Marani, M. (2010). Geomorphological origin of recession curves. *Geophysical Research Letters*, *37*, L24403. https://doi.org/10.1029/2010GL045415

Biswal, B., & Nagesh Kumar, D. (2014). Study of dynamic behaviour of recession curves. *Hydrological Processes*, *28*(3), 784–792. https://doi.org/10.1002/hyp.9604

Blyth, K., & Rodda, J. (1973). A stream length study. *Water Resources Research*, *9*(5), 1464–1461. https://doi.org/10.1029/WR009i005p01454

Boodoo, K. S., Trauth, N., Schmidt, C., Schelker, J., & Battin, T. J. (2017). Gravel bars are sites of increased CO_2 outgassing in stream corridors. *Scientific Reports*, *7*(1), 1–9. https://doi.org/10.1038/s41598-017-14439-0

BotterG., & DurighettoN. (2020). The stream length duration curve: A tool for characterizing the time variability of the flowing stream length. *Water Resources Research*, *56*, e2020WR027282. https://doi.org/10.1029/2020WR027282

Botter, G., Porporato, A., Rodriguez-Iturbe, I., & Rinaldo, A. (2009). Nonlinear storage–discharge relations and catchment streamflow regimes. *Water Resources Research*, *45*, W10427. https://doi.org/10.1029/2008WR007658

Burnham, K. P., & Anderson, D. R. (2002). *Model selection and multimodel inference: A practical information—Theoretic approach* (2nd ed., pp. 490). Springer-Verlag.

Costigan, K. H., Daniels, M. D., & Dodds, W. K. (2015). Fundamental spatial and temporal disconnections in the hydrology of an intermittent prairie headwater network. *Journal of Hydrology*, *522*, 305–316. https://doi.org/10.1016/j.jhydrol.2014.12.031

Costigan, K. H., Jaeger, K. L., Goss, C. W., Fritz, K. M., & Goebel, P. C. (2016). Understanding controls on flow permanence in intermittent rivers to aid ecological research: Integrating meteorology, geology and land cover. *Ecohydrology*, *9*(7), 1141–1153. https://doi.org/10.1002/eco.1712

Datry, T., Foulquier, A., Corti, R., Von Schiller, D., Tockner, K., Mendoza-Lera, C., et al. (2018). A global analysis of terrestrial plant litter dynamics in non-perennial waterways. *Nature Geoscience*, *11*(7), 497–503. https://doi.org/10.1038/s41561-018-0134-4

Datry, T., Larned, S. T., & Tockner, K. (2014). Intermittent rivers: A challenge for freshwater ecology. *BioScience*, *64*, 229–235. https://doi.org/10.1093/biosci/bit027

Datry, T., Pella, H., Leigh, C., Bonada, N., & Hugueny, B. (2016). A landscape approach to advance intermittent river ecology. *Freshwater Biology*, *61*(8), 1200–1213. https://doi.org/10.1111/fwb.12645

Day, D. (1978). Drainage density changes during rainfall. *Earth Surface Processes*, *3*, 319–326. https://doi.org/10.1002/esp.3290030310

Day, D. (1980). Lithologic controls of drainage density: A study of six small rural catchments in New England, N.S.W. *Catena*, *7*, 339–351. https://doi.org/10.1016/S0341-8162(80)80024-5

Doering, M., Uehlinger, U., Rotach, A., Schlaepfer, D. R., & Tockner, K. (2007). Ecosystem expansion and contraction dynamics along a large Alpine alluvial corridor (Tagliamento River, Northeast Italy). *Earth Surface Processes and Landforms*, *32*(11), 1693–1704. https://doi.org/10.1002/esp.1594

Downing, J. A., Cole, J. J., Duarte, C. M., Middelburg, J. J., Melack, J. M., Prairie, Y. T., et al. (2012). Global abundance and size distribution of streams and rivers. *Inland Waters*, *2*, 229–236. https://doi.org/10.5268/IW-2.4.502

Dupas, R., Abbott, B., Minaudo, C., & Fovet, O. (2019). Distribution of landscale units within catchments influences nutrient export dynamics. *Frontiers in Environmental Science*, *7*, 43. https://doi.org/10.3389/fenvs.2019.00043

Durighetto, N., Vingiani, F., Bertassello, L. E., Camporese, M., & Botter, G. (2020). Intraseasonal drainage network dynamics in a headwater catchment of the Italian Alps. *Water Resources Research*, *56*, e2019WR025563. https://doi.org/10.1029/2019WR025563

European Commission. (2000). *Directive 2000/60/EC of the European Parliament and of the Council of 23 October 2000 establishing a framework for community action in the field of water policy*. Office for Official Publications of the European Communities.

Fekete, B. M., & Vörösmarty, C. J. (2007). The current status of global river discharge monitoring and potential new technologies complementing traditional discharge measurements. *IAHS Publication*, *309*, 129–136.

Floriancic, M. G., van Meerveld, I., Smoorenburg, M., Margreth, M., Naef, F., Kirchner, J. W., & Molnar, P. (2018). Spatio-temporal variability in contributions to low flows in the high Alpine Poschiavino catchment. *Hydrological Processes*, *32*(26), 3938–3953. https://doi.org/10.1002/hyp.13302

Fritz, K. M., Hagenbuch, E., D'Amico, E., Reif, M., Wigington, P. J., Jr., Leibowitz, S. G., et al. (2013). Comparing the extent and permanence of headwater streams from two field surveys to values from hydrographic databases and maps. *JAWRA Journal of the American Water Resources Association*, *49*(4), 867–882. https://doi.org/10.1111/jawr.12040

Garcia, C., Amengual, A., Homar, V., & Zamora, A. (2017). Losing water in temporary streams on a Mediterranean island: Effects of climate and land-cover changes. *Global and Planetary Change*, *148*, 139–152. https://doi.org/10.1016/j.gloplacha.2016.11.010

Godsey, S., & Kirchner, J. (2014). Dynamic, discontinuous stream networks: Hydrologically driven variations in active drainage density, flowing channels and stream order. *Hydrological Processes*, *28*, 5791–5803. https://doi.org/10.1002/hyp.10310

González-Ferreras, A. M., & Barquín, J. (2017). Mapping the temporary and perennial character of whole river networks. *Water Resources Research*, *53*, 6709–6724. https://doi.org/10.1002/2017WR020390

Goulsbra, C., Evans, M., & Lindsay, J. (2014). Temporary streams in a peatland catchment: Pattern, timing, and controls on stream network expansion and contraction. *Earth Surface Processes and Landforms*, *39*(6), 790–803. https://doi.org/10.1002/esp.3533

Gregory, K., & Gardiner, V. (1979). Comment on drainage density and streamflow: A closer look by S. L. Dingman. *Water Resources Research*, *15*(6), 1662–1664. https://doi.org/10.1029/WR015i006p01662

Gregory, K., & Walling, D. (1968). The variation of drainage density within a catchment. *International Association of Scientific Hydrology Bulletin*, *13*, 61–68. https://doi.org/10.1080/02626666809493583

Guisan, A., Weiss, S. B., & Weiss, A. D. (1999). GLM versus CCA spatial modeling of plant species distribution. *Plant Ecology*, *143*(1), 107–122. https://doi.org/10.1023/A:1009841519580

Jaeger, K. L., Montgomery, D. R., & Bolton, S. M. (2007). Channel and perennial flow initiation in headwater streams: Management implications of variability in source-area size. *Environmental Management*, *40*(5), 775. https://doi.org/10.1007/s00267-005-0311-2

Jaeger, K. L., Sando, R., McShane, R. R., Dunham, J. B., Hockman-Wert, D. P., Kaiser, K. E., et al. (2019). Probability of Streamflow Permanence Model (PROSPER): A spatially continuous model of annual streamflow permanence throughout the Pacific Northwest. *Journal of Hydrology X*, *2*, 100005. https://doi.org/10.1016/j.hydroa.2018.100005

Jensen, C., McGuire, K., & Prince, P. (2017). Headwater stream length dynamics across four physiographic provinces of the Appalachian Highlands. *Hydrological Processes*, *31*, 3350–3363. https://doi.org/10.1002/hyp.11259

Jensen, C. K., McGuire, K. J., McLaughlin, D. L., & Scott, D. T. (2019). Quantifying spatiotemporal variation in headwater stream length using flow intermittency sensors. *Environmental Monitoring and Assessment*, *191*(4), 226. https://doi.org/10.1007/s10661-019-7373-8

Jensen, C. K., McGuire, K. J., Shao, Y., & Andrew Dolloff, C. (2018). Modeling wet headwater stream networks across multiple flow conditions in the Appalachian Highlands. *Earth Surface Processes and Landforms*, *43*(13), 2762–2778. https://doi.org/10.1002/esp.4431

Jenson, S. K., & Domingue, J. O. (1988). Extracting topographic structure from digital elevation data for geographic information system analysis. *Photogrammetric Engineering & Remote Sensing*, *54*(11), 1593–1600.

Kaplan, N. H., Blume, T., & Weiler, M. (2020). Predicting probabilities of streamflow intermittency across a temperate mesoscale catchment. *Hydrology and Earth System Sciences*, *24*(11), 5453–5472. https://doi.org/10.5194/hess-24-5453-2020

Kaplan, N. H., Sohrt, E., Blume, T., & Weiler, M. (2019). Monitoring ephemeral, intermittent and perennial streamflow: A dataset from 182 sites in the Attert catchment, Luxembourg. *Earth System Science Data*, *11*, 1363–1374. https://doi.org/10.5194/essd-11-1363-2019

Kim, S., & Sharma, A. (2019). The role of floodplain topography in deriving basin discharge using passive microwave remote sensing. *Water Resources Research*, *55*, 1707–1716. https://doi.org/10.1029/2018WR023627

Köppen, W. (1936). Das geographisca System der Klimate. In W. Köppen & G. Geiger (Eds.), Handbuch der Klimatologie (Vol. 1). Gebruder Borntraeger. Retrieved from https://koeppen-geiger.vu-wien.ac.at/pdf/Koppen_1936.pdf

Larned, S. T., Datry, T., Arscott, D. B., & Tockner, K. (2010). Emerging concepts in temporary-river ecology. *Freshwater Biology*, *5*, 717–738. https://doi.org/10.1111/j.1365-2427.2009.02322.x

Li, J., & Wong, D. W. (2010). Effects of DEM sources on hydrologic applications. *Computers, Environment and Urban Systems*, *34*, 251–261. https://doi.org/10.1016/j.compenvurbsys.2009.11.002

Lovill, S. M., Hahm, W. J., & Dietrich, W. E. (2018). Drainage from the critical zone: Lithologic controls on the persistency and spatial extent of wetted channels during the summer dry season. *Water Resources Research*, *54*, 5702–5726. https://doi.org/10.1029/2017WR021903

Malard, F., Uehlinger, U., Zah, R., & Tockner, K. (2006). Flood-pulse and riverscape dynamics in a braided glacial river. *Ecology*, *87*(3), 704–716. https://doi.org/10.1890/04-0889

McInerney, D., Kavetski, D., Thyer, M., Lerat, J., & Kuczera, G. (2019). Benefits of explicit treatment of zero flows in probabilistic hydrological modeling of ephemeral catchments. *Water Resources Research*, *55*, 11035–11060. https://doi.org/10.1029/2018WR024148

Medici, C., Butturini, A., Bernal, S., Vázquez, E., Sabater, F., Vélez, J. I., & Francés, F. (2008). Modelling the non-linear hydrological behaviour of a small Mediterranean forested catchment. *Hydrological Processes: AnInternational Journal*, *22*(18), 3814–3828. https://doi.org/10.1002/hyp.6991

Mendicino, G. (1999). Sensitivity analysis on GIS procedures for the estimate of soil erosion risk. *Natural Hazards*, *20*(2–3), 231–253. https://doi.org/10.1023/A:1008120231103

Mendicino, G., & Colosimo, F. (2019). Analysis of flow resistance equations in gravel-bed rivers with intermittent regimes: Calabrian fiumare data set. *Water Resources Research*, *55*, 7294–7319. https://doi.org/10.1029/2019WR024819

Mendicino, G., & Senatore, A. (2013a). Evaluation of parametric and statistical approaches for the regionalization of flow duration curves in intermittent regimes. *Journal of Hydrology*, *480*, 19–32. https://doi.org/10.1016/j.jhydrol.2012.12.017

Mendicino, G., & Senatore, A. (2013b). Regionalization of the Hargreaves coefficient for the assessment of distributed reference evapotranspiration in southern Italy. *Journal of Irrigation and Drainage Engineering*, *139*(5), 349–362. https://doi.org/10.1061/(ASCE)IR.1943-4774.0000547

Mendicino, G., & Sole, A. (1997). The information content theory for the estimation of the topographic index distribution used in TOPMODEL. *Hydrological Processes*, *11*(9), 1099–1114. https://doi.org/10.1002/(SICI)1099-1085(199707)11:9<1099::AID-HYP547>3.0.CO;2-F

Morgan, R. (1972). Observations on factors affecting the behaviour of a first-order stream. *Transactions of the Institute of British Geographers*, *56*, 171–185. https://doi.org/10.2307/621547

Nikolaidis, N. P., Demetropoulou, L., Froebrich, J., Jacobs, C., Gallart, F., Prat, N., et al. (2013). Towards sustainable management of Mediterranean river basins: Policy recommendations on management aspects of temporary streams. *Water Policy*, *15*(5), 830–849. https://doi.org/10.2166/wp.2013.158

Paillex, A., Siebers, A. R., Ebi, C., Mesman, J., & Robinson, C. T. (2020). High stream intermittency in an alpine fluvial network: Val Roseg, Switzerland. *Limnology & Oceanography*, *65*(3), 557–568. https://doi.org/10.1002/lno.11324

Payn, R. A., Gooseff, M. N., McGlynn, B. L., Bencala, K. E., & Wondzell, S. M. (2012). Exploring changes in the spatial distribution of stream baseflow generation during a seasonal recession. *Water Resources Research*, *48*, W04519. https://doi.org/10.1029/2011WR011552

Peirce, S. E., & Lindsay, J. B. (2015). Characterizing ephemeral streams in a southern Ontario watershed using electrical resistance sensors. *Hydrological Processes*, *29*(1), 103–111. https://doi.org/10.1002/hyp.10136

Perez, A. B. A., Innocente dos Santos, C., Sá, J. H. M., Arienti, P. F., & Chaffe, P. L. B. (2020). Connectivity of ephemeral and intermittent streams in a subtropical Atlantic forest headwater catchment. *Water*, *12*, 1526. https://doi.org/10.3390/w12061526

Phillips, R. W., Spence, C., & Pomeroy, J. W. (2011). Connectivity and runoff dynamics in heterogeneous basins. *Hydrological Processes*, *25*(19), 3061–3075. https://doi.org/10.1002/hyp.8123

Prancevic, J. P., & Kirchner, J. W. (2019). Topographic controls on the extension and retraction of flowing streams. *Geophysical Research Letters*, *46*, 2084–2092. https://doi.org/10.1029/2018GL081799

Reddyvaraprasad, C., Patnaik, S., & Biswal, B. (2020). Recession flow prediction in gauged and ungauged basins by just considering past discharge information. *Hydrological Sciences Journal*, *65*(1), 21–32. https://doi.org/10.1080/02626667.2019.1643465

Reyjol, Y., Argillier, C., Bonne, W., Borja, A., Buijse, A. D., Cardoso, A. C., et al. (2014). Assessing the ecological status in the context of the European Water Framework Directive: Where do we go now? *The Science of the Total Environment*, *497*, 332–344. https://doi.org/10.1016/j.scitotenv.2014.07.119

Roberts, M. C., & Archibold, O. W. (1978). Variation of drainage density in a small British Columbia watershed 1. *JAWRA Journal of the American Water Resources Association*, *14*(2), 470–476. https://doi.org/10.1111/j.1752-1688.1978.tb02183.x

Schiller, D. V., Marcé, R., Obrador, B., Gómez-Gener, L., Casas-Ruiz, J. P., Acuña, V., & Koschorreck, M. (2014). Carbon dioxide emissions from dry watercourses. *Inland Waters*, *4*(4), 377–382. https://doi.org/10.5268/IW-4.4.746

Senatore, A., Mendicino, G., Smiatek, G., & Kunstmann, H. (2011). Regional climate change projections and hydrological impact analysis for a Mediterranean basin in southern Italy. *Journal of Hydrology*, *399*(1–2), 70–92. https://doi.org/10.1016/j.jhydrol.2010.12.035

Senatore, A., Micieli, M., Liotti, A., Durighetto, N., Mendicino, G., & Botter, G. (2020). *Monitoring and modeling drainage network contraction and dry down in Mediterranean headwater catchments* [data collection]. Retrieved from http://researchdata.cab.unipd.it/id/eprint/375

Shaw, S. B. (2016). Investigating the linkage between streamflow recession rates and channel network contraction in a mesoscale catchment in New York state. *Hydrological Processes*, *30*(3), 479–492. https://doi.org/10.1002/hyp.10626

Shaw, S. B., Bonville, D. B., & Chandler, D. G. (2017). Combining observations of channel network contraction and spatial discharge variation to inform spatial controls on baseflow in Birch Creek, Catskill Mountains, USA. *Journal of Hydrology: Regional Studies*, *12*, 1–12. https://doi.org/10.1016/j.ejrh.2017.03.003

Skoulikidis, N. T., Sabater, S., Datry, T., Morais, M. M., Buffagni, A., Dörflinger, G., et al. (2017). Non-perennial Mediterranean rivers in Europe: Status, pressures, and challenges for research and management. *The Science of the Total Environment*, *577*, 1–18. https://doi.org/10.1016/j.scitotenv.2016.10.147

Spence, C., & Mengistu, S. (2016). Deployment of an unmanned aerial system to assist in mapping an intermittent stream. *Hydrological Processes*, *30*(3), 493–500. https://doi.org/10.1002/hyp.10597

Tomaštík, J., Mokroš, M., Surový, P., Grznárová, A., & Merganič, J. (2019). UAV RTK/PPK method—An optimal solution for mapping inaccessible forested areas? *Remote Sensing*, *11*(6), 721. https://doi.org/10.3390/rs11060721

Tooth, S. (2000). Process, form and change in dryland rivers: A review of recent research. *Earth-Science Reviews*, *5*, 67–107. https://doi.org/10.1016/S0012-8252(00)00014-3

Tortorici, L., Monaco, C., Tansi, C., & Cocina, O. (1995). Recent and active tectonics in the Calabrian Arc (south Italy). *Tectonophysics*, *243*, 37–55. https://doi.org/10.1016/0040-1951(94)00190-k

Van Meerveld, H. J., Kirchner, J. W., Vis, M. J., Assendelft, R. S., & Seibert, J. (2019). Expansion and contraction of the flowing stream network alter hillslope flowpath lengths and the shape of the travel time distribution. *Hydrology and Earth System Sciences*, *23*(11), 4825–4834. https://doi.org/10.5194/hess-23-4825-2019

Vander Vorste, R., Sarremejane, R., & Datry, T. (2019). Intermittent rivers and ephemeral streams: A unique biome with important contributions to biodiversity and ecosystem services. In *Reference module in Earth systems and environmental sciences* (pp. 419–429). Elsevier. https://doi.org/10.1016/B978-0-12-409548-9.12054-8

Ward, A. S., Schmadel, N. M., & Wondzell, S. M. (2018). Simulation of dynamic expansion, contraction, and connectivity in a mountain stream network. *Advances in Water Resources*, *114*, 64–82. https://doi.org/10.1016/j.advwatres.2018.01.018

Whiting, J. A., & Godsey, S. E. (2016). Discontinuous headwater stream networks with stable flowheads, Salmon River basin, Idaho. *Hydrological Processes*, *30*(13), 2305–2316. https://doi.org/10.1002/hyp.10790

Wigington, P. J., Jr., Moser, T. J., & Lindeman, D. R. (2005). Stream network expansion: A riparian water quality factor. *Hydrological Processes: An International Journal*, *19*(8), 1715–1721. https://doi.org/10.1002/hyp.5866

Yu, S., Bond, N. R., Bunn, S. E., Xu, Z., & Kennard, M. (2018). Quantifying spatial and temporal patterns of flow intermittency using spatially contiguous runoff data. *Journal of Hydrology*, *559*, 861–872. https://doi.org/10.1016/j.jhydrol.2018.03.009

Zehe, E., & Sivapalan, M. (2009). Threshold behaviour in hydrological systems as (human) geo-ecosystems: Manifestations, controls, implications. *Hydrology and Earth System Sciences*, *13*, 1273–1297. https://doi.org/10.5194/hess-13-1273-2009

Zimmer, M. A., Kaiser, K. E., Blaszczak, J. R., Zipper, S. C., Hammond, J. C., Fritz, K. M., et al. (2020). Zero or not? Causes and consequences of zero-flow stream gage readings. *WIREs Water*, *7*(3), e1436. https://doi.org/10.1002/wat2.1436

Zimmer, M. A., & McGlynn, B. L. (2017). Ephemeral and intermittent runoff generation processes in a low relief, highly weathered catchment. *Water Resources Research*, *53*, 7055–7077. https://doi.org/10.1002/2016WR019742

Zimmer, M. A., & McGlynn, B. L. (2018). Lateral, vertical, and longitudinal source area connectivity drive runoff and carbon export across watershed scales. *Water Resources Research*, *54*, 1576–1598. https://doi.org/10.1002/2017WR021718